nature communications

Article

https://doi.org/10.1038/s41467-025-68068-7

Unconventional polaronic ground state in superconducting $LiTi_2O_4$

Received: 3 January 2025

Accepted: 16 December 2025

Published online: 06 January 2026

Check for updates

Zubia Hasan[1,16], Grace A. Pan[1,16], Harrison LaBollita[2], Austin Kaczmarek[3], Suk Hyun Sung[4], Shekhar Sharma[2], Purnima P. Balakrishnan[5], Edward Mercer[6,7], Vivek Bhartiya[8], Alpha T. N'Diaye[9], Zaher Salman[10], Thomas Prokscha[10], Andreas Suter[10], Alexander J. Grutter[5], Mirian Garcia-Fernandez[11], Ke-Jin Zhou[11], Jonathan Pelliciari[8], Valentina Bisogni[8], Ismail El Baggari[4], Darrell G. Schlom[12,13,14,15], Matthew R. Barone[12], Charles M. Brooks[1], Katja C. Nowack[3], Antia S. Botana[2], Brendan D. Faeth[12], Alberto de la Torre[6,7] ✉ & Julia A. Mundy[1] ✉

Geometrically frustrated lattices can display a range of correlated phenomena, ranging from spin frustration and charge order to dispersionless flat bands due to quantum interference. One particularly compelling family of such materials is the half-valence spinel LiB_2O_4 materials. On the *B*-site frustrated pyrochlore sublattice, the interplay of correlated metallic behavior and charge frustration leads to a superconducting state in $LiTi_2O_4$ and heavy fermion behavior in LiV_2O_4. To date, however, $LiTi_2O_4$ has primarily been understood as a conventional BCS superconductor despite a lattice structure that could host more exotic ground states. Here, we present a multimodal investigation of $LiTi_2O_4$, combining ARPES, RIXS, proximate magnetic probes, and ab-initio many-body theoretical calculations. Our data reveals a novel mobile polaronic ground state with spectroscopic signatures that underlie co-dominant electron-phonon coupling and electron-electron correlations also found in the lightly doped cuprates. The cooperation between the two interaction scales distinguishes $LiTi_2O_4$ from other superconducting titanates, suggesting an unconventional origin to superconductivity in $LiTi_2O_4$. Our work deepens our understanding of the rare interplay of electron-electron correlations and electron-phonon coupling in unconventional superconducting systems. In particular, our work identifies the geometrically frustrated, mixed-valence spinel family as an underexplored platform for discovering unconventional, correlated ground states.

The interplay between electron–electron correlations and electron–phonon coupling has been of long-standing interest in understanding superconductivity. In traditional Bardeen-Cooper-Schrieffer (BCS) superconductors, Coulomb repulsion between electrons is thought to screen electron-phonon coupling and reduce the superconducting transition temperature T_c[1]. In unconventional superconductors, however, there can be a more complex interplay between electron–phonon coupling and electron–electron interactions. Strong correlations can further strengthen the electron-phonon coupling and enhance T_c[2–4]. In certain cases, as explored for cuprates[5], the energy scales of strong electron–electron correlations can overwhelm those of electron–phonon interactions, leading to charge and spin fluctuations that compete with or enhance superconductivity[6]. Thus, understanding how electronic correlations and electron–phonon coupling interact in

A full list of affiliations appears at the end of the paper. ✉e-mail: a.delatorreduran@northeastern.edu; mundy@fas.harvard.edu

https://doi.org/10.1038/s41467-025-68068-7

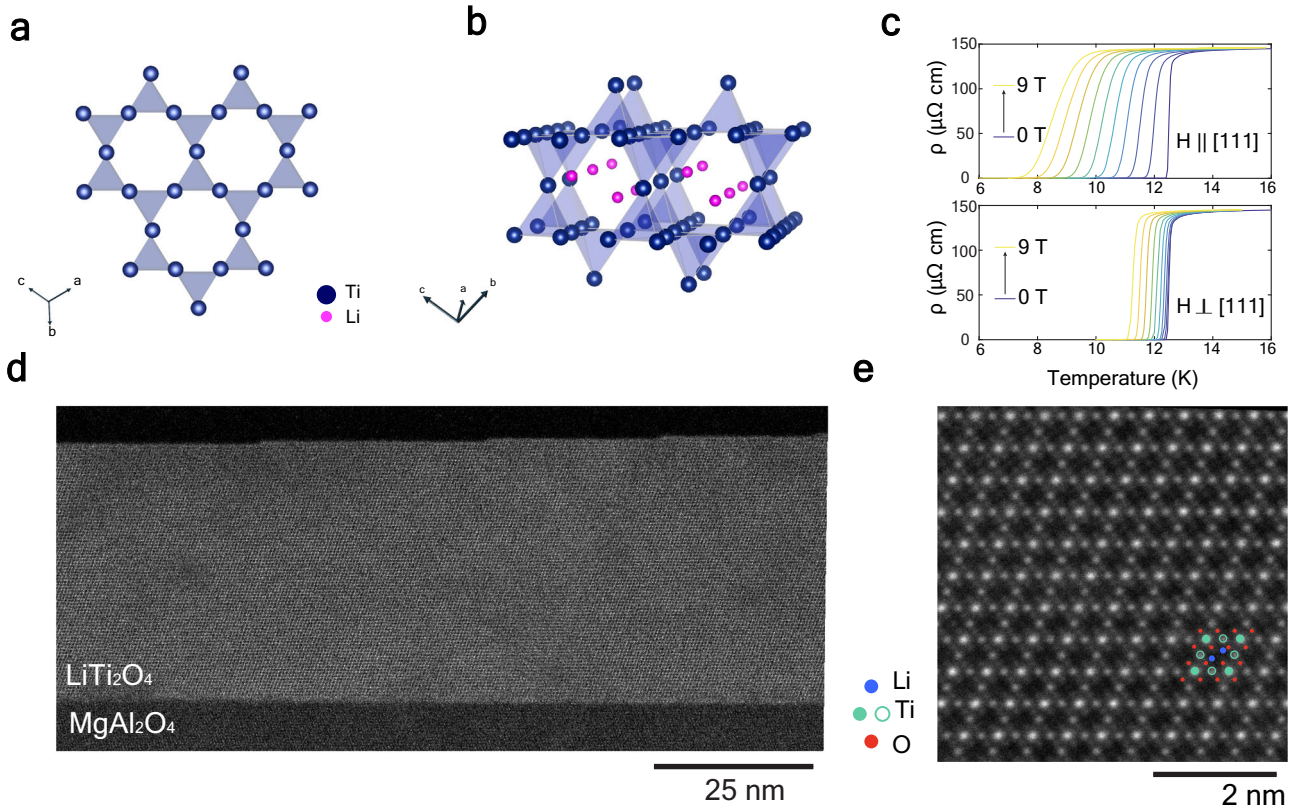

Fig. 1 | Structural and electrical characterization of $LiTi_2O_4$. a The (111) plane of $LiTi_2O_4$ showing the titanium kagome sublattice inherent to the spinel structure. **b** Side-view of the (111) plane shown in **a**, highlighting the three-dimensional nature of the geometric frustration in $LiTi_2O_4$. **c** Resistivity ρ vs temperature of $LiTi_2O_4$ with magnetic field (0 to 9 T) parallel and perpendicular to the sample. **d** Large field-of-view HAADF-STEM image of $LiTi_2O_4$ showing uniform crystallinity over a large area. **e** Local HAADF-STEM image of $LiTi_2O_4$ overlaid with the corresponding atoms.

superconductors is important in identifying new families of unconventional superconductors and ascertaining the mechanisms behind high-temperature superconductivity.

Although superconductivity was discovered in $LiTi_2O_4$ before the cuprates[7], it remains a unique instance of a spinel superconductor and with the highest T_c for a mixed-valence titanate. In this crystal structure, $d^{0.5}$ titanium atoms form a pyrochlore sublattice, composed of alternating planes of Kagome and triangles (Fig. 1a, b). While this geometric construction has given rise to strong electron correlations in other systems[8], these interactions have been largely unexplored in $LiTi_2O_4$. Indeed, superconductivity in $LiTi_2O_4$ has primarily been considered as phonon-mediated BCS-like, supported by specific heat, tunneling spectroscopy, and muon spin rotation measurements[9–11]. In contrast, anomalous magnetotransport behavior and scanning tunneling spectroscopy experiments have suggested the presence of spin fluctuations, orbital ordering, and pseudo-gap-like states in $LiTi_2O_4$, all of which are typically associated with unconventional superconductors and strongly correlated materials[10,12,13]. Interestingly, previous theoretical studies of $LiTi_2O_4$ have suggested non-BCS-like superconducting mechanisms, such as bipolaronic[14,15] or resonating valence bond (RVB) superconductivity[16,17]. While there have been speculations about the role of electron–electron correlations[9,18], a more detailed investigation into the strength and nature of various correlations is needed to explore the notion of "unconventional superconductivity" in $LiTi_2O_4$.

Here, we reveal the complex interplay between electron–phonon coupling and electron–electron interactions in $LiTi_2O_4$. We use molecular-beam epitaxy (MBE) to synthesize epitaxial thin films of superconducting $LiTi_2O_4$, enabling a detailed spectroscopic investigation using resonant inelastic x-ray scattering (RIXS) and angle-resolved photoemission spectroscopy (ARPES). The combination of the element-specific sensitivity to structural and local excitations of RIXS, together with the unique capability of ARPES to reveal energy and momentum dependence of the quasiparticle self-energy, enables us to provide a comprehensive description of the low-energy physics of $LiTi_2O_4$. We observe evidence of strong electronic correlations and signatures of strong electron–phonon coupling. The cooperation between these two interaction scales gives rise to a novel polaronic ground state—also found in weakly doped cuprates[19]—that dynamically localizes titanium states in $LiTi_2O_4$. This interpretation is further supported by our theoretical calculations, which can reproduce some of the spectral features in our ARPES data when considering electron correlations or electron–phonon interactions separately, but are unable to reproduce polaronic phenomena associated with the interplay of both interactions. Our work thus challenges the notion of phonon-dominated BCS superconductivity in $LiTi_2O_4$ by revealing the complex correlations present in this material, hearkening comparisons to cuprate-like physics.

Results

Synthesis and characterization of superconducting $LiTi_2O_4$

Thin films of $LiTi_2O_4$ were grown via reactive oxide MBE on (111)-oriented $MgAl_2O_4$ substrates (see "Methods"). As shown in Fig. 1c, the films display a superconducting transition with T_c ~ 12.5 K and a residual resistivity ratio (RRR) of ~ 5.85 (Fig. S3), consistent with previous reports of the highest quality $LiTi_2O_4$[7,10]. Figure 1d, e show high-angle annular dark field scanning transmission electron microscopy (HAADF-STEM) images of $LiTi_2O_4$, attesting to the high structural quality of our films (also see Supplementary Fig. S1).

Additionally, we confirm the onset of superconductivity and probe the superconducting order parameter using scanning

https://doi.org/10.1038/s41467-025-68068-7

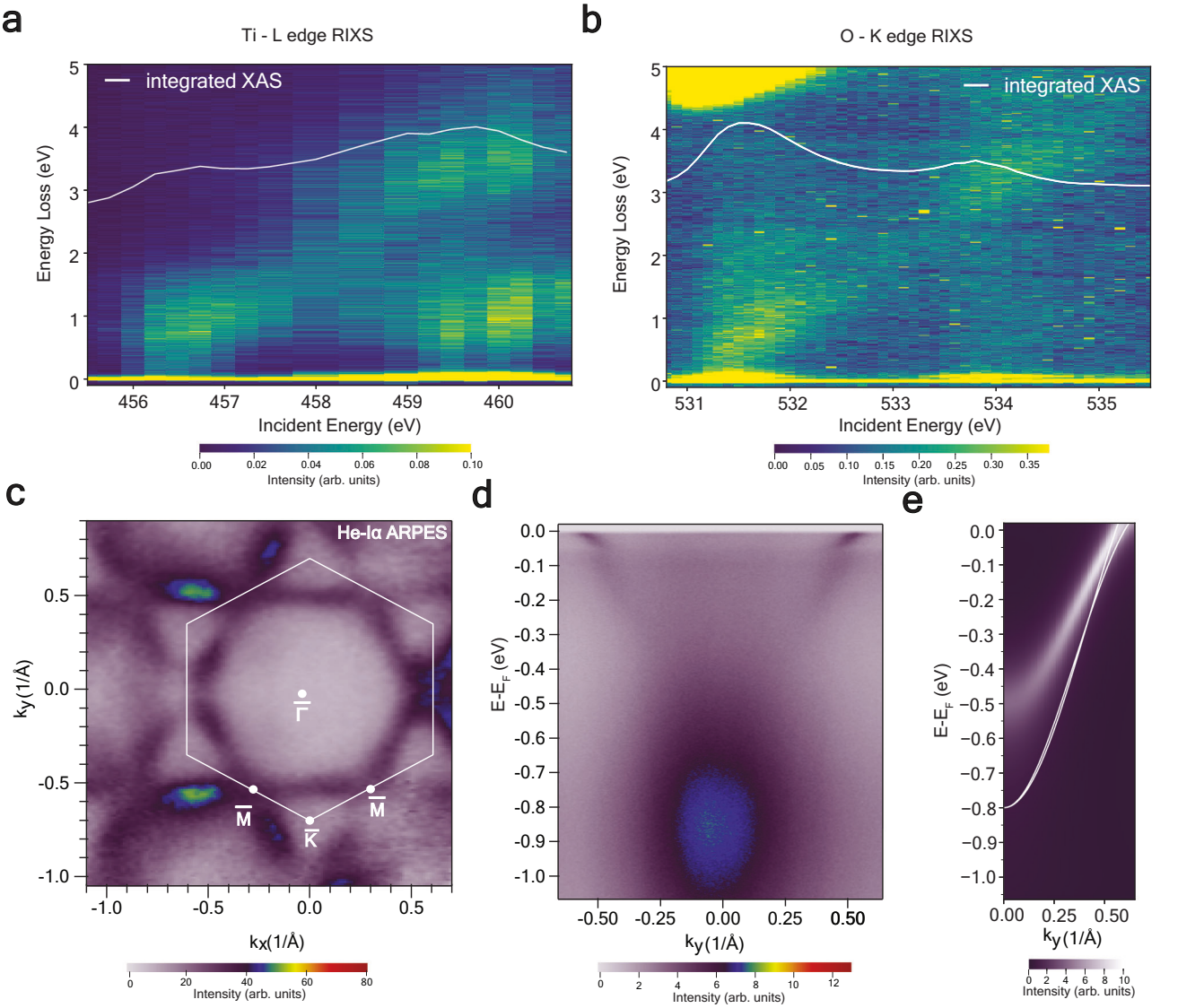

Fig. 2 | Electron–electron correlations in $LiTi_2O_4$. **a** RIXS intensity at the Ti-L_3 edge. **b** RIXS intensity at the O K-edge. **c** Iso-energy map at the Fermi level taken with He-Iα showing a hexagonal Fermi surface. The white hexagon indicates the first Brillouin zone. **d** Experimental band structure in the $\bar{K} - \bar{\Gamma} - \bar{K}$ direction. **e** DMFT and DFT (white) comparison along $\bar{\Gamma} - \bar{K}$ indicating the mass renormalization due to electron–electron correlations.

superconducting quantum interference device (SQUID) microscopy, which locally measures magnetic susceptibility (Fig. S4). The measured magnetic susceptibility can be used to extract the temperature dependence of the reduced London penetration depth (Supplementary Material Section S3), which can be well-fit by a fully gapped order parameter, consistent with *s*-wave-like pairing. The observation of the 2-D thin film limit of superconductivity, the high RRR, as well as a homogeneous diamagnetic response from scanning SQUID, demonstrates the high structural quality of our films, ensuring that further measurements probe the intrinsic behavior of $LiTi_2O_4$.

Electron–electron correlations in $LiTi_2O_4$

Poised with high-quality thin films, we first probe the electronic structure using elemental-specific RIXS measurements. Figure 2a shows the RIXS intensity of $LiTi_2O_4$ near the Ti-L_3 edge. Our x-ray absorption spectroscopy (XAS) data (Fig. S16a) display resonant features associated with the mixed valence Ti^{4+} and Ti^{3+} states (for a detailed discussion on the mixed-valence XAS, see Supplementary Section S9). Given the lack of *dd* excitations expected for a trivial d^0 state, we conclude that the broad Raman-like *dd* features centered at $E_{loss} = 1.5$ eV and $E_{loss} = 4$ eV, reflect a d^1 titanium occupation state, which, given the lack of charge order in $LiTi_2O_4$, can only be dynamically populated[20]. These Raman-like excitations, along with the suppressed fluorescence contribution, are unexpected, given that the itinerant charge carriers in our metallic and superconducting samples are proposed to have a dominant Ti-3*d* band character near the Fermi level[21,22]. We note that our RIXS data resemble that of $MgTi_2O_4$[23] despite $LiTi_2O_4$ lacking large static local trigonal distortions of the TiO_6 octahedra and Ti-Ti dimerization (Supplementary Figs. S1 and S22). The qualitative similarities between the RIXS energy maps in metallic $LiTi_2O_4$ and Mott-insulating systems like $MgTi_2O_4$ are suggestive of the presence of localized excitations in $LiTi_2O_4$.

In addition to the Raman-like excitations, we observe spectral weight associated with a fluorescence contribution with a linear dispersion in E_i that extends below $E_{loss} \leq 1.5$ eV. This resembles the superposition of localized and delocalized excitations observed in negative charge transfer insulators[24]. Moreover, O K-edge RIXS, shown in Fig. 2b, also shows Raman-like and fluorescence contributions below the charge transfer gap, $\Delta \approx 4.5$ eV. This is the same energy as the intra-*dd* excitations at the Ti L_3-edge, suggesting strong hybridization

https://doi.org/10.1038/s41467-025-68068-7

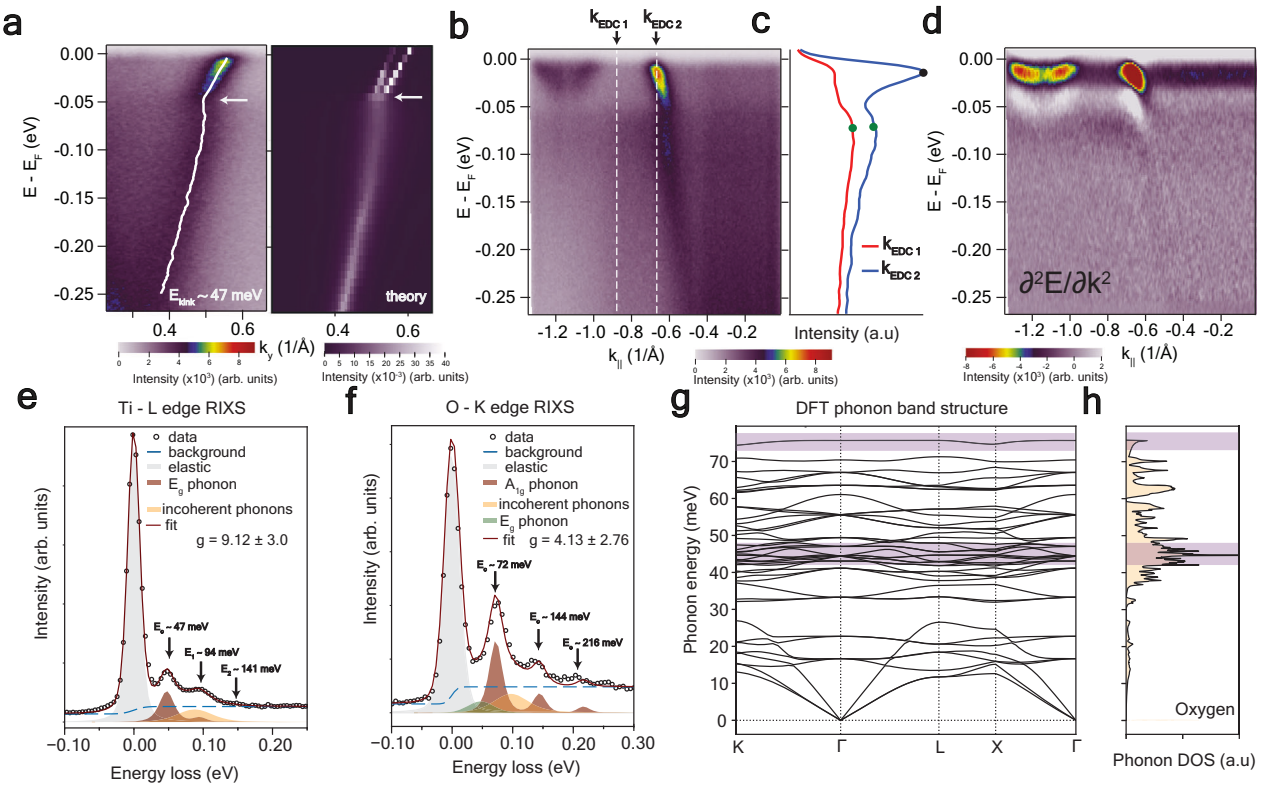

Fig. 3 | Electron–phonon coupling in $LiTi_2O_4$. **a** Comparison of the $\bar{\Gamma}-\bar{K}$ ARPES data to density-functional perturbation theory (DFPT) highlighting the kink feature at 47 meV at $\bar{\Gamma}-\bar{K}$ at $T = 7$ K. **b** Energy - momentum ARPES spectra along the $\bar{\Gamma}-\bar{K}-\bar{M}$ direction. **c** EDC cuts at two different $k_{||}$ highlighted in (**b**) with dotted white lines. Black and green dots correspond to the top of the two EDC poles. **d** Second-derivative plot from (**b**) highlighting a dispersionless spectral intensity at the second pole denoted by a black arrow in (**c**) also observable in the raw data in (**b**). A spectral gap is also prominent at the same energy scale where the dispersionless feature interrupts the main band. **e** Quasi-elastic RIXS excitations shown at $E_{inc} = 460$ eV for the Ti-L_3 edge. **f** Quasi-elastic RIXS excitations shown at $E_{inc} = 531.5$ eV for the O K-edge. The total intensity is a fit (red solid line) to a Voigt peak (gray shading), a background step function (blue dashed lines), one (two) Gaussian(s) and an Ament model fit to the phonon spectra (maroon) in (**e**), (**f**), respectively. **g**, **h** Calculated phonon band structure and total oxygen phonon density of states, respectively. The purple box highlights the energy scale of the A_{1g} and E_g modes, respectively, in both plots.

between titanium and oxygen carriers. While the hybridization between Ti-3*d* and O-2*p* states has been previously theorized[21], the RIXS data is the first instance of direct observation of strong titanium-oxygen hybridization. Moreover, the presence of fluorescence contributions at the O-*K*-edge near the elastic line (zero energy loss) suggests a larger contribution of oxygen carriers to electronic transport in $LiTi_2O_4$ than that expected from previous density of states calculations[21]. Thus, our RIXS data suggest the presence of charge localization, Ti-3*d* and O-2*p* hybridization, and electron–electron correlations in $LiTi_2O_4$.

Electron–electron correlations are also observed in in-situ ARPES measurements on $LiTi_2O_4$. Figure 2c shows the Fermi surface of $LiTi_2O_4$ from our ARPES measurements. Here, k_x and k_y are chosen to lie along the $[11\bar{2}]$ and $[\bar{1}10]$ directions, respectively. The Fermi surface is characterized by large electron pockets with hexagonal symmetry centered at Γ, pushing toward the zone boundary in proximity to a Lifshitz transition, which has led to enhanced electronic interactions near the Fermi surface for other superconductors[25]. A more detailed discussion of the Fermi surface and its k_z dependence is given in Supplementary Figs. S5, S6 and in the Supplementary Material Section S4.

To analyze the electronic interactions, we look at high-symmetry cuts of the band structure of $LiTi_2O_4$. In Fig. 2d, e, we compare our experimental band structure along $\bar{\Gamma}-\bar{K}$ to the momentum-resolved spectral function obtained from density-functional theory plus dynamical mean-field theory (DFT+DMFT). The non-interacting band dispersion is shown in white in Fig. 2e for reference. The DFT+DMFT calculation reproduces the experimental dispersion near Γ, capturing the large effective mass renormalization compared to the bare DFT band—a clear indication of strong electron correlations in $LiTi_2O_4$. The calculated cyclotron mass (Supplementary Material Fig. S9) yields $\frac{m_{eff}}{m_{bare}} = 2.53 \pm 0.4$. This method of calculating the renormalization agrees with previous reports of the effective mass of $LiTi_2O_4$ by other optical probes[26,27]. Additionally, we observe a broad Gaussian-like, intense incoherent spectral weight centered at $E_B \approx 0.9$ eV that resembles the lower Hubbard band of lightly doped cuprates[28]. Similar to the cuprates, the spectral weight shows k_z dependence with a transition from a "champagne glass-like dispersion" to a "waterfall" feature[29] in the data taken by Ne-Iα photon energy (16.85 eV) (Supplementary Fig. S6b). We note this feature cannot be reproduced by DMFT calculations but is consistent with a previous photoemission spectroscopy measurement of $LiTi_2O_4$, where it was interpreted as a signature of polaronic behavior[14]. Nonetheless, our combined ARPES and RIXS data provide the first observation of significant electronic correlations in $LiTi_2O_4$.

Electron–phonon coupling in $LiTi_2O_4$

While electronic correlations play a key role in unconventional superconductivity, we also observe signatures of electron–phonon coupling in the electronic structure of $LiTi_2O_4$. Consistent with previous ARPES reports[30], we observe a "kink" at $E_B \approx 46$ meV as shown in Fig. 3a. This feature is ascribed to an E_g oxygen phonon mode by tunneling spectroscopy measurements[31] and inelastic neutron scattering[32], confirmed by calculations of the spectral function including the self-energy from only electron–phonon interactions

(Supplementary Material Section S5). We extract a band renormalization, $\lambda_{tot} = 1.80(1)$, three times higher than $\lambda_{e-ph} = 0.65$ determined by specific heat measurements[9] and ab-initio calculations[18]. The extracted band renormalization value from our ARPES data is comparable to that from electronic specific heat measurements, where the larger value is attributed to enhancement from electron–electron correlations or spin fluctuations[22,33,34]. We note that λ_{tot} includes λ_{e-ph} as well as λ_{e-e}. While a precise determination of just λ_{e-ph} is non-trivial due to the interlinked nature of electron–electron correlations and electron–phonon coupling in this compound, we can approximate $\lambda_{e-ph} \approx 1.3 \pm 0.5$ by fitting the dispersion of the band at lower binding energies as the bare band, consistent with λ_{e-ph} extracted from other ARPES measurements on this compound[30]. For a more detailed discussion on the calculation of λ_{tot} and λ_{e-ph} as well as their temperature and momentum dependence, see Supplementary Material Section S4 and Fig. S7.

Figure 3b shows an energy-momentum cut along the $\bar{\Gamma} - \bar{K} - \bar{M}$ direction (cut overlaid on the Brillouin zone is shown in Fig. S8a). Here we observe a non-dispersive feature at $E_B = 70.4 \pm 6$ meV at all $k_{||}$, highlighting the accumulation of incoherent spectral weight below the main kink at $E = 46$ meV (Fig. 3a). To examine this flat feature, we present two energy dispersive cuts (EDC) in Fig. 3c, k_{EDC1} which cuts across momentum value devoid of bands and k_{EDC2} which cuts across the k_F of the main $LiTi_2O_4$ band. The momentum position of these two cuts is indicated by two black arrows pointing to dotted white lines in Fig. 3b. We can see the peak position of this sub-band in the EDC of k_{EDC1} as an abrupt and sharp increase in spectral intensity at $\Omega = 70.4 \pm 6$ meV (green dot), also observed in k_{EDC2} at the same energy scale. Sub-bands like these are indicative of a highly interacting picture[35], in stark contrast to a non-interacting picture, where, in the absence of any bands, the expected EDC would not have any additional poles, unlike what is seen in k_{EDC1}. The second derivative plot (Fig. 3d) further highlights this feature and additionally shows a “spectral gap" where the non-dispersive feature interrupts the main dispersive electronic band. We note that the flat feature, in addition to the spectral gap, can also be seen clearly in our raw data in Fig. 2d. These types of sub-bands due to strong electron-phonon coupling are spectral signatures that are consistent with the formation of intra-unit cell small polarons[36] that have been observed in other correlated materials[35,37].

Our RIXS measurements also corroborate the presence of strong electron-phonon coupling and multiphonon processes in $LiTi_2O_4$. Figure 3e shows the RIXS spectra at the Ti L_3- and O K-edges, respectively. As highlighted by black arrows in Fig. 3e, f, both RIXS spectra are characterized by prominent quasi-elastic peaks that are approximately equally spaced and monotonically decay with E_{loss}, thus resembling the harmonic progression of the multiphononic processes. The low-energy excitations shown in the titanium spectra are well fit by the Ament model[38], which considers a single non-dispersive phonon mode coupled to the electronic structure with strength g (See Supplementary Material Section S6 for more details on the Ament model fit). At the Ti-L_3 edge, the Ament model in conjunction with a broad Gaussian peak centered at $E_{loss} = 90$ meV provides a good fit for a mode centered at $\Omega = 47 \pm 2$ meV, in agreement with the oxygen E_g mode observed in ARPES. We interpret this broad Gaussian peak to represent multiple incoherent phononic excitations that cannot be resolved within the energy resolution of the instrument, also observed in $MgTi_2O_4$[23].

The coupling strength, $g_{Ti} = 9.1 \pm 3.0$, far exceeds those of other titanates[39,40], and is on par with some cuprates measured via RIXS[41] further supporting strong electron-phonon coupling in $LiTi_2O_4$. Moreover, the observation of a pure oxygen E_g mode at the titanium edge is indicative of strong hybridization between the O-2p and the Ti-3d orbitals. Similar to the Ti L_3-edge, the three excitations at the O K-edge can also be well fit by the Ament model in conjunction with two broad Gaussian peaks. The fit gives us the first three harmonics of a phonon mode centered at $\Omega = 72 \pm 1$ meV with $g_O = 4.13 \pm 2.76$. We assign this mode to the oxygen A_{1g} phonon, which is known to be strongly coupled to the E_g mode[18]. While the A_{1g} mode is coherent at the O K-edge, the broad Gaussian centered at $E \approx 46$ meV, which encodes the coupling to the E_g mode also seen at the Ti L-edge, indicates a reduced coherence of this mode at the O K-edge. The absence of higher harmonics of the E_g mode at the O K-edge might be due to the higher density of oxygen modes at that energy, as shown in Fig. 3h (For a detailed discussion on the different phonon modes, see Supplementary Section 6). We note that our DFT calculations of the phonon band structure (Fig. 3g) show the modes around $\Omega \approx 46$ meV and ≈ 75 meV to be relatively nondispersive, supporting our choice of Ament model fitting for the quasi-elastic peaks at the Ti L_3- and O K-edges.

Discussion

Our combined spectroscopic data indicate that the effects of electron–electron correlations and electron-phonon coupling cannot be disentangled in $LiTi_2O_4$. Moreover, ab-initio calculations (Figs. 2e and 3a) treating electron-phonon coupling and electron–electron correlations separately fail to capture the most salient features of our data, namely the existence of localized excitations in $LiTi_2O_4$ (Fig. 2a) and the presence of a second pole in the photoemission self-energy (Fig. 3c). While the combined theoretical description of these two energy scales remains challenging and a matter of active research[42], there is growing evidence that the excitation spectrum, band structure and transport properties of quantum materials such as $SrVO_3$[43] and superconductors like alkalli-fullerides[37] and the cuprates[44] can only by understood through the interplay of both interaction scales. We note that while competing interactions are generally associated with unconventional superconductivity, our scanning SQUID data are consistent with a conventional s-wave order parameter (Supplementary Section S3). This naturally also raises the question as to how the phonon-mediated attractive interaction—essential for s-wave superconductivity—is robust against or potentially enhanced by the repulsive electronic correlations apparent in $LiTi_2O_4$. Within this context, $LiTi_2O_4$ departs from $SrTiO_3$[45] and other superconducting titanates[46,47] where electron-phonon coupling is understood to be the dominant interaction.

We finally comment on the possible mechanism that enables the strong interplay of electron–electron and electron-phonon interactions in $LiTi_2O_4$. In this context, it is instructive to consider the $d^{0.5}$ occupation state in $LiTi_2O_4$ in the context of the d^1 member of the AB_2O_4 family, $MgTi_2O_4$. In $MgTi_2O_4$, a trigonal distortion driven by E_g and A_{1g} oxygen phonons[48] lifts the orbital degeneracy of the Ti $3d^1$ state in a perfect cubic octahedral environment (Fig. 4a, b). The combination of this local distortion with the formation of Ti-Ti dimers at $T = 260$ K[48] leads to a tetragonal, dimerized unit cell and the formation of a correlated insulating state (Fig. 4b) in $MgTi_2O_4$. In the $d^{0.5}$ mixed-valence state, the energy gain from dimerization is reduced in favor of a charge-ordered ground state, such as in mixed-valence spinel $CuIr_2S_4$[49]. However, no static symmetry breaking due to orbital or lattice ordering has been reported in $LiTi_2O_4$[10], possibly due to the geometric frustration inherent in the spinel structure. This raises the question of how the d^1 state, with its associated local distortion, is accommodated in $LiTi_2O_4$. We speculate that in $LiTi_2O_4$ with an occupation $d^{0.5}$ in the absence of charge order, two titanium ions share an electron dynamically, such that their occupation state fluctuates between d^1 and d^0. In this scenario, the transiently occupied d^1 site has an associated local symmetry reduction due to dynamic lattice fluctuations of the E_g and A_{1g} oxygen phonons, as seen in $MgTi_2O_4$[50]. As the electron moves to the unoccupied d^0 site, it drags the local distortion with it, leading to the formation of a polaronic state in which charge motion and lattice distortions are coupled (Fig. 4b). Notably, this polaronic mechanism for Ti^{3+} defect induced carriers in a Ti^{4+} system has already been proposed for $Li_4Ti_5O_{12}$[51], suggesting a similar

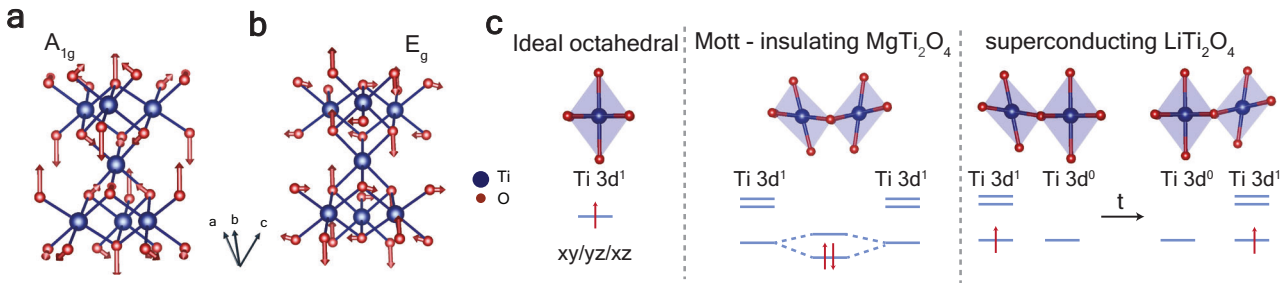

Fig. 4 | Polaron formation in $LiTi_2O_4$. a, b DFT calculated A_{1g} and E_g oxygen phonon modes in $LiTi_2O_4$. **c** An ideal TiO_6 octahedra (left) with a highly degenerate d^1 state in a cubic crystal field. In $MgTi_2O_4$, a local trigonal distortion driven by E_g and A_{1g} phonons is required to achieve a dimerized ground state (middle). Dynamic symmetry-reducing local lattice fluctuations associated with electron hopping leading to polaron formation in $LiTi_2O_4$ (right).

mechanism for polaronic transport in $LiTi_2O_4$ where the mixed-valence is native to the material.

Our data reflect the formation of such a small mobile polaronic state in $LiTi_2O_4$. First, our ARPES data show a strong coupling ($\lambda > 1$) to a non-dispersive E_g phonon mode. The ratio of the dominant E_g phonon mode energy (Ω = 46 meV), to the bare electron bandwidth ($t \approx 800$ meV), places $LiTi_2O_4$in the adiabatic limit ($\Omega/t << 1$) for which the condition $\lambda > 1$ is expected for a small polaron ground state[52]. Second, the observation of the same mode (E_g, oxygen mode) at the Ti-L_3 edge indicates a tightly hybridized state between the localized d^1 titanium electrons and the deformed lattice. Third, we observe large incoherent spectral weight at $E \approx 0.9$ eV, which cannot be accounted for by either of our density-functional perturbation theory (DFPT) or DMFT calculations. We note that polaronic behavior has been previously discussed for $LiTi_2O_4$ based on the anomalous transport behavior of off-stoichiometric samples[53] and previous photoemission and reflectance spectroscopy data[14,54]. Notably, the metallic behavior of $LiTi_2O_4$ at all temperatures contrasts with the localized small Holstein polaron behavior of other titanates[55,56] where a low-temperature insulating state occurs due to reduced lattice mobility. However, in the light regime ($m^* < 10m$), small polarons have been theoretically predicted to be mobile[57,58]. Polaron delocalization involves a crawling-like motion in which an electron is transiently delocalized over two neighboring sites[59], similar to the mechanism suggested here for the $d^{0.5}$ state in $LiTi_2O_4$ (Fig. 4b), in which the dynamical lattice fluctuations are coupled to electron hopping between d^1 and d^0 states. We note that this mobile polaron formation requires an intricate balance between electron–electron correlations and electron-phonon coupling. Dominant electron–electron correlations may choose a charge-ordered ground state[49] while dominant electron-phonon coupling can lead to bi-polaron formation, as suggested for other titanates, like Ti_4O_7[56]. Thus, our data suggests a serendipitous balancing of electron–electron correlations with electron-phonon coupling in this material.

Although $LiTi_2O_4$ has long been thought of as a well-studied BCS superconductor consistent with phonon-dominated superconductivity as in other titanates[46,47], our work forces us to reconsider the notion of conventional superconductivity in $LiTi_2O_4$. Here, a re-examination of $LiTi_2O_4$ using ARPES and RIXS measurements uncovers strong hybridization between titanium and oxygen, considerable electron–electron correlations, and co-existing electron-phonon coupling. In mixed valence $LiTi_2O_4$, this balance of energy scales results in a novel mobile polaronic ground state indicative of a unique balance of charge delocalization, electron–electron correlations, and electron-phonon coupling. $LiTi_2O_4$ becomes a model system to explore predictions of enhancement of superconductivity due to the cooperative effect of electron–electron correlations and electron-phonon coupling in the quarter-filled Hubbard Hamiltonian[60]. Moreover, the proximity of superconductivity to an orbitally ordered phase, the correlated behavior, and the strong hybridization between titanium and oxygen highlight a rich competition between energy scales found only in special classes of quantum materials. Our work expands our understanding of superconductivity in $d^{0.5}$ systems and demonstrates how mixed-valence spinel-oxide structures can host correlated physics, thus broadening our search for material families that can host such correlated phenomena.

Methods

Synthesis of $LiTi_2O_4$ thin films via MBE

We used reactive oxide molecular beam epitaxy (Veeco GEN 10) to synthesize thin film $LiTi_2O_4$ on untreated $MgAl_2O_4$ (111) substrates (CrysTec GmbH). The lithium and titanium fluxes were matched and set to ~1.5×10^{13} atoms/cm^2·s as measured by a quartz crystal microbalance (QCM). We obtained the lithium flux by flowing O_2 during the QCM process and forming Li_2O, as the low atomic mass of elemental lithium yields small frequency changes on the QCM below the detection sensitivity, except for at very high fluxes. For the deposition process, we heated the substrates with a 10.6 μm CO_2 laser to 825 °C in a pressure of $1.0–2.0 \times 10^{-7}$ molecular O_2 over a chamber background pressure of ~5.0×10^{-8}. We co-deposited the lithium and titanium sources for 1 h. After deposition, we shut off the O_2 flow to prevent oxidation of titanium to the 4+ state and cooled at a rate of 100 °C/min.

Structural characterization

Annular dark field (ADF) STEM was performed on Thermofisher Scientific (TFS) Themis (operated at 200 keV, convergence semi-angle 18.9 mrad, ADF collection angle: 36–200 mrad). A small ADF inner collection angle was used to increase light element sensitivity. Electron-transparent TEM samples were prepared using TFS Helios DualBeam FIB/SEM.

Transport measurements

We performed all electrical transport measurements in a Hall bar geometry using evaporated Cr/Au (7 nm/100 nm) contacts with the Hall channel defined by a diamond scribe along the [11-2] crystallographic direction of the $MgAl_2O_4$ (111) substrate. We loaded the samples in 9 T Dynacool Physical Property Measurement System (PPMS) and used AC lock-in techniques at ~15 Hz.

Resonant inelastic X-ray scattering

The XAS and RIXS spectra were collected at the SIX beamline at NSLS-II and the I21 beamline of Diamond Light Source. The Ti L_3-edge was measured at SIX and I21, while the O K-edge spectra were acquired at I21. The Ti L_3-edge energy map is collected at $2\theta = 150°$, while the O K-edge energy map is collected at $2\theta = 90°$. All RIXS spectra are collected at $2\theta = 90°$ at grazing incidence of $\theta = 20°$ unless indicated otherwise. The energy resolution was fixed between 20 to 25 meV at both SIX and Diamond, respectively. All data were measured at a base temperature of 22K at both beamlines.

Angle-resolved photoemission spectroscopy

All in situ photoemission measurements were conducted by immediately transferring the samples through a UHV manifold ($P < 2 \times 10^{-9}$ Torr) to a measurement chamber immediately following film growth. ARPES measurements were taken with a Scienta Omicron DA30-L electron analyzer equipped with a Fermion Instruments BL1200s multi-gas discharge lamp using He-I photons at 21.2 eV, Ne-I photons at 16.85 eV, and He-II photons at 40.2 eV. The base pressure in the ARPES system is maintained during measurements at pressures lower than 5×10^{-11} Torr. ARPES measurements were performed at a temperature of 7K and a nominal experimental energy resolution of 10 meV unless otherwise indicated.

Muon spin relaxation measurements

Low-energy muon spin-relaxation (LE-μSR) measurements were done using the LEM instrument at the Swiss muon source. An applied field of 10 mT was applied transverse to the μ^+s spin polarization direction. For more details on the μSR measurements, refer to Supplementary Material Section S7.

X-ray absorption spectroscopy

XAS of uncapped $LiTi_2O_4$ thin films was performed at 300 K at Beamline 6.3.1 at the Advanced Light Source at Lawrence Berkeley National Laboratory. XAS of capped $LiTi_2O_4$ thin films was performed at 300 K at ID-32 at Diamond Light Source. The spectra from Beamline 6.3.1 represent an average of 4 individual scans. All spectra are taken in the total electron yield configuration. The $LiTi_2O_4$ XAS spectra do not show any polarization dependence. For more details on the XAS, refer to Supplementary Material Section S9.

Data availability

All data used to obtain the conclusions in this paper are presented in the paper and/or the Supplementary Materials. This data may be requested from the authors. Please direct all inquiries to Z.H. (zhasan@g.harvard.edu).

References

1. Matthias, B. T. Chapter V Superconductivity in the Periodic System. *In Progress in Low Temperature Physics*, Vol. 2, 138–150. (C. J. Gorter, ed.) (Elsevier, 1957).
2. Capone, M., Fabrizio, M., Castellani, C. & Tosatti, E. Strongly correlated superconductivity. *Science* **296**, 2364–2366 (2002).
3. Yuan, Z. et al. Correlation-enhanced electron-phonon coupling and superconductivity in (Ba, K)SbO_3 superconductors. *Phys. Rev. B* **105**, 014517 (2022).
4. Nomura, Y., Sakai, S., Capone, M. & Arita, R. Unified understanding of superconductivity and Mott transition in alkali-doped fullerides from first principles. *Sci. Adv.* **1**, e1500568 (2015).
5. Scalapino, D. J. A common thread: the pairing interaction for unconventional superconductors. *Rev. Mod. Phys.* **84**, 1383–1417 (2012).
6. van Loon, E. G. C. P., Rösner, M., Schönhoff, G., Katsnelson, M. I. & Wehling, T. O. Competing coulomb and electron-phonon interactions in NbS_2. *npj Quantum Mater.* **3**, 1–8 (2018).
7. Johnston, D. C. Superconducting and normal state properties of $Li_{1+x}Ti_{2-x}O_4$ spinel compounds. i. preparation, crystallography, superconducting properties, electrical resistivity, dielectric behavior, and magnetic susceptibility. *J. Low. Temp. Phys.* **25**, 145–175 (1976).
8. Wakefield, J. P. et al. Three-dimensional flat bands in pyrochlore metal $CaNi_2$. *Nature* **623**, 301–306 (2023).
9. Sun, C. P. et al. Magnetic field dependence of low-temperature specific heat of the spinel oxide superconductor $LiTi_2O_4$. *Phys. Rev. B* **70**, 054519 (2004).
10. Jin, K. et al. Anomalous magnetoresistance in the spinel superconductor $LiTi_2O_4$. *Nat. Commun.* **6**, 7183 (2015).
11. Wu, W. D. et al. Magnetic penetration depth in V_3Si and $LiTi_2O_4$ measured by μSR. *Hyperfine Interact.* **86**, 615–621 (1994).
12. Okada, Y. et al. Scanning tunnelling spectroscopy of superconductivity on surfaces of $LiTi_2O_4$(111) thin films. *Nat. Commun.* **8**, 15975 (2017).
13. Xue, H. et al. Fourfold symmetric superconductivity in spinel oxide $LiTi_2O_4$(001) thin films. *ACS Nano* **16**, 19464–19471 (2022).
14. Edwards, P. P. et al. A study of the spinel materials $LiTi_2O_4$ and $Li_{43}Ti_{53}O_4$ by photoelectron spectroscopy. *J. Solid State Chem.* **54**, 127–135 (1984).
15. Alexandrov, A. & Ranninger, J. Bipolaronic superconductivity. *Phys. Rev. B* **24**, 1164–1169 (1981).
16. Anderson, P. W. The resonating valence bond state in La_2CuO_4 and superconductivity. *Science* **235**, 1196–1198 (1987).
17. Anderson, P. W., Baskaran, G., Zou, Z. & Hsu, T. Resonating-valence-bond theory of phase transitions and superconductivity in La_2CuO_4-based compounds. *Phys. Rev. Lett.* **58**, 2790–2793 (1987).
18. Oda, T., Shirai, M., Suzuki, N. & Motizuki, K. Electron-phonon interaction, lattice dynamics and superconductivity of an oxide spinel $LiTi_2O_4$. *J. Phys. Condens. Matter* **6**, 6997 (1994).
19. Shen, K. M. et al. Missing quasiparticles and the chemical potential puzzle in the doping evolution of the cuprate superconductors. *Phys. Rev. Lett.* **93**, 267002 (2004).
20. Iwahara, N. & Shikano, S. Vibronic excitations in resonant inelastic x-ray scattering spectra of K_2RuCl_6. *Phys. Rev. Res.* **5**, 023051 (2023).
21. Massidda, S., Yu, J. & Freeman, A. J. Electronic structure and properties of superconducting $LiTi_2O_4$. *Phys. Rev. B* **38**, 11352–11357 (1988).
22. Satpathy, S. & Martin, R. M. Electronic structure of the superconducting oxide spinel $LiTi_2O_4$. *Phys. Rev. B* **36**, 7269–7272 (1987).
23. Li, Q. et al. Evolution of orbital excitations from insulating to superconducting $MgTi_2O_4$ films. *Phys. Rev. B* **107**, L121108 (2023).
24. Bisogni, V. et al. Ground-state oxygen holes and the metal–insulator transition in the negative charge-transfer rare-earth nickelates. *Nat. Commun.* **7**, 13017 (2016).
25. Shi, X. et al. Enhanced superconductivity accompanying a Lifshitz transition in electron-doped FeSe monolayer. *Nat. Commun.* **8**, 14988 (2017).
26. Ohsawa, T. et al. Origin of optical transparency in a transparent superconductor $LiTi_2O_4$. *ACS Appl. Electron. Mater.* **2**, 517–522 (2020).
27. Zhao, M. et al. Pseudo-dielectric functions, band-to-band transitions, and dielectric-related factors in a single-crystal $LiTi_2O_4$ thin film. *Opt. Mater.* **142**, 114034 (2023).
28. Myasnikova, A. E., Zhileeva, E. A. & Moseykin, D. V. Relaxation of strongly coupled electron and phonon fields after photoemission and high-energy part of ARPES spectra of cuprates. *J. Phys. Condens. Matter* **30**, 125601 (2018).
29. Inosov, D. S. et al. Excitation energy map of high-energy dispersion anomalies in cuprates. *Phys. Rev. B Condens. Matter Mater. Phys.* **77**, 212504 (2008).
30. Fujisawa, Y. et al. Imaging emergent exotic quasiparticle states in a frustrated transition metal oxide. Preprint at https://doi.org/10.48550/arXiv.2306.06708(2023).
31. Gilmore, K. et al. Description of resonant inelastic X-ray scattering in correlated metals. *Phys. Rev. X* **11**, 031013 (2021).
32. Green, M. A., Dalton, M., Prassides, K., Day, P. & Neumann, D. A. Lattice vibrations of the superconducting oxide spinels. *J. Phys. Condens. Matter* **9**, 10855–10865 (1997).
33. Heintz, J. M. et al. Superconductivity of $LiTi_2O_4$ and related systems. *Z. Phys. B Condens. Matter* **76**, 303–309 (1989).

34. McCallum, R. W., Johnston, D. C., Luengo, C. A. & Maple, M. B. Superconducting and normal state properties of $Li_{1+x}Ti_{2-x}O_4$ spinel compounds. ii. low-temperature heat capacity. *J. Low. Temp. Phys.* **25**, 177–193 (1976).
35. Kang, M. et al. Holstein polaron in a valley-degenerate two-dimensional semiconductor. *Nat. Mater.* **17**, 676–680 (2018).
36. Hohenadler, M., Aichhorn, M. & Von Der Linden, W. Spectral function of electron-phonon models by cluster perturbation theory. *Phys. Rev. B* **68**, 184304 (2003).
37. Zhou, J. S. et al. Evidence for band renormalizations in strong-coupling superconducting alkali-fulleride films. *Phys. Rev. Lett.* **130**, 216004 (2023).
38. Ament, L. J. P., Van Veenendaal, M. & Van Den Brink, J. Determining the electron-phonon coupling strength from Resonant Inelastic X-ray Scattering at transition metal L-edges. *Europhys. Lett.* **95**, 27008 (2011).
39. Moser, S. et al. Electron-phonon coupling in the bulk of anatase TiO_2 measured by resonant inelastic x-ray spectroscopy. *Phys. Rev. Lett.* **115**, 096404 (2015).
40. Fatale, S., Moser, S., Miyawaki, J., Harada, Y. & Grioni, M. Hybridization and electron-phonon coupling in ferroelectric $BaTiO_3$ probed by resonant inelastic x-ray scattering. *Phys. Rev. B* **94**, 195131 (2016).
41. Braicovich, L. et al. Determining the electron-phonon coupling in superconducting cuprates by resonant inelastic x-ray scattering: methods and results on $Nd_{1+x}Ba_{2-x}Cu_3O_{7-\delta}$. *Phys. Rev. Res.* **2**, 023231 (2020).
42. Abramovitch, D. J., Zhou, J. J., Mravlje, J., Georges, A. & Bernardi, M. Combining electron-phonon and dynamical mean-field theory calculations of correlated materials: transport in the correlated metal Sr_2RuO_4. *Phys. Rev. Mater.* **7**, 093801 (2023).
43. Abramovitch, D. J., Mravlje, J., Zhou, J. J., Georges, A. & Bernardi, M. Respective roles of electron-phonon and electron-electron interactions in the transport and quasiparticle properties of $SrVO_3$. *Phys. Rev. Lett.* **133**, 186501 (2024).
44. He, Y. et al. Rapid change of superconductivity and electron-phonon coupling through critical doping in Bi-2212. *Science* **362**, 62–65 (2018).
45. Wang, Z. et al. Tailoring the nature and strength of electron-phonon interactions in the SrTiO3(001) 2D electron liquid. *Nat. Mater.* **15**, 835–839 (2016).
46. Zhang, C. et al. Enhanced superconductivity in TiO epitaxial thin films. *npj Quantum Mater.* **2**, 1–5 (2017).
47. Yoshimatsu, K., Sakata, O. & Ohtomo, A. Superconductivity in Ti_4O_7 and γ-Ti_3O_5 films. *Sci. Rep.* **7**, 12544 (2017).
48. Popović, Z. V. et al. Phonon properties of the spinel oxide $MgTi_2O_4$ with the S= 1/2 pyrochlore lattice. *Phys. Rev. B* **68**, 224302 (2003).
49. Radaelli, P. G. et al. Formation of isomorphic Ir^{3+} and Ir^{4+} octamers and spin dimerization in the spinel $CuIr_2S_4$. *Nature* **416**, 155–158 (2002).
50. Yang, L. et al. Two-orbital degeneracy lifted local precursor to a metal-insulator transition in $MgTi_2O_4$. *Phys. Rev. B* **102**, 235128 (2020).
51. Kick, M., Grosu, C., Schuderer, M., Scheurer, C. & Oberhofer, H. Mobile small polarons qualitatively explain conductivity in lithium titanium oxide battery electrodes. *J. Phys. Chem. Lett.* **11**, 2535–2540 (2020).
52. Capone, M., Ciuchi, S and Grimaldi, C. The small polaron crossover: role of dimensionality. In *Stripes and Related Phenomena*, 169–174 (Springer, 2000).
53. Watanabe, M., Kaneda, K., Takeda, H. & Tsuda, N. Semiconducting properties of $Li_{1.1}Ti_{1.9}O_4$. *J. Phys. Soc. Jpn.* **53**, 2437–2440 (1984).
54. Harrison, M. R., Edwards, P. P. & Goodenough, J. B. A study of the $Li_{1+x}Ti_{2-x}O_4$ spinel system by diffuse reflectance spectroscopy. *J. Solid State Chem.* **54**, 426–437 (1984).
55. Yang, S., Brant, A. T., Giles, N. C. & Halliburton, L. E. Intrinsic small polarons in rutile TiO_2. *Phys. Rev. B* **87**, 125201 (2013).
56. Lakkis, S., Schlenker, C., Chakraverty, B. K., Buder, R. & Marezio, M. Metal-insulator transitions in Ti_4O_7 single crystals: Crystal characterization, specific heat, and electron paramagnetic resonance. *Phys. Rev. B* **14**, 1429–1440 (1976).
57. Davenport, A. R., Hague, J. P. & Kornilovitch, P. E. Mobile small bipolarons on a three-dimensional cubic lattice. *Phys. Rev. B Condens. Matter Mater. Phys.* **86**, 035106 (2012).
58. Hague, J. P., Kornilovitch, P. E., Samson, J. H. & Alexandrov, A. S. Superlight small bipolarons in the presence of a strong coulomb repulsion. *Phys. Rev. Lett.* **98**, 037002 (2007).
59. Holstein, T. Studies of polaron motion: Part ii. the "small" polaron. *Ann. Phys.* **8**, 343–389 (1959).
60. Clay, R. T. & Roy, D. Superconductivity due to cooperation of electron-electron and electron-phonon interactions at quarter filling. *Phys. Rev. Res.* **2**, 023006 (2020).

Acknowledgements

We thank useful discussions with G. Grissonnanche, M. R. Norman, Y. Wang, F. Baumberger, and J. Sous. This research is primarily supported by the National Science Foundation, Division of Materials Research, under Award No. DMR-2339913. Materials growth and photoemission studies were supported by the Platform for the Accelerated Realization, Analysis, and Discovery of Interface Materials (PARADIM) under NSF Cooperative Agreement No. DMR-2039380. All nanofabrication work was performed at Harvard University's Center for Nanoscale Systems (CNS), a member of the National Nanotechnology Coordinated Infrastructure Network (NNCI), supported by the National Science Foundation under NSF Grant No. 2025158. Z.H. and G.A.P. acknowledge support from the Paul & Daisy Soros Fellowship for New Americans. G.A.P. acknowledges additional support from the NSF Graduate Research Fellowship Grant No. DGE-1745303. A.K. and K.C.N. acknowledge support from the Air Force Research Laboratory, Project Grant FA95502110429. S.H.S. and I.E.B. acknowledge support from the Rowland Institute at Harvard University. J.A.M. acknowledges support from the Packard Foundation and the Sloan Foundation. This research used beamline 2-ID of the National Synchrotron Light Source II, which is a US DOE Office of Science Facility operated for the DOE Office of Science by Brookhaven National Laboratory under contract no. DE-SC0012704. HL and ASB acknowledge support from NSF Grant No. DMR-2323971. The μSR experiments were performed at the Swiss Muon Source, SμS, Paul Scherrer Institute, Villigen, Switzerland. Certain commercial equipment, instruments, software, or materials are identified in this paper in order to specify the experimental procedure adequately. Such identifications are not intended to imply recommendation or endorsement by NIST, nor are they intended to imply that the materials or equipment identified are necessarily the best available for the purpose. This research used resources of the Advanced Light Source, which is a DOE Office of Science User Facility under contract no. DE-AC02-05CH11231.

Author contributions

Z.H., G.A.P., C.M.B., and J.A.M. synthesized the thin films with assistance from M.R.B. and D.G.S. Electrical transport measurements were performed and analyzed by G.A.P. Scanning transmission electron microscopy was performed by S.H.S. and I.E. ARPES measurements were performed by Z.H., G.A.P., and B.D.F. ARPES analysis was done by Z.H. and B.D.F. with support from A.d.l.T. The RIXS measurements were performed by Z.H., E.M., S.H.S., I.B., and A.d.l.T. with support from V.B., J.P., M.G.F., and K.Z. RIXS analysis was done by Z.H., S.H.S., and E.M under the supervision of A.d.l.T. XAS measurements were supported by A.T.N. μSR measurements were performed by A.J.G. and P.P.B. with support from A.S., Z.S., and T.P. Analysis of μSR data was done by A.J.G. and P.P.B. Scanning SQUID measurements were performed by A.K. and K.C.N. H.L., S.S., and A.S.B. performed the DFT, DMFT, and electron-

phonon calculations. J.A.M. and A.d.l.T. conceived and guided the study. Z.H., G.A.P., J.A.M., and A.d.l.T. wrote the manuscript with contributions and discussion from all authors.

Competing interests
The authors declare no competing interests.

Additional information
Supplementary information The online version contains supplementary material available at https://doi.org/10.1038/s41467-025-68068-7.

Correspondence and requests for materials should be addressed to Alberto de la Torre or Julia A. Mundy.

Peer review information *Nature Communications* thanks the anonymous reviewers for their contribution to the peer review of this work. A peer review file is available.

Reprints and permissions information is available at http://www.nature.com/reprints

Publisher's note Springer Nature remains neutral with regard to jurisdictional claims in published maps and institutional affiliations.

[1]Department of Physics, Harvard University, Cambridge, MA, USA. [2]Department of Physics, Arizona State University, Tempe, AZ, USA. [3]Laboratory of Atomic and Solid-State Physics, Cornell University, Ithaca, NY, USA. [4]The Rowland Institute, Harvard University, Cambridge, MA, USA. [5]NIST Center for Neutron Research, National Institute for Standards and Technology, Gaithersburg, MD, USA. [6]Department of Physics, Northeastern University, Boston, MA, USA. [7]Quantum Materials and Sensing Institute, Northeastern University, Burlington, MA, USA. [8]National Synchrotron Light Source II, Brookhaven National Laboratory, Upton, NY, USA. [9]Advanced Light Source, Lawrence Berkeley National Laboratory, Berkeley, CA, USA. [10]PSI Center for Neutron and Muon Sciences, Villigen, Switzerland. [11]Diamond Light Source, Harwell Campus, Didcot, UK. [12]Platform for the Accelerated Realization, Analysis, and Discovery of Interface Materials (PARADIM), Cornell University, Ithaca, NY, USA. [13]Department of Materials Science and Engineering, Cornell University, Ithaca, NY, USA. [14]Kavli Institute at Cornell for Nanoscale Science, Ithaca, NY, USA. [15]Leibniz-Institut für Kristallzüchtung, Berlin, Germany. [16]These authors contributed equally: Zubia Hasan, Grace A. Pan. ✉e-mail: a.delatorreduran@northeastern.edu; mundy@fas.harvard.edu

Supplemental Material for: Unconventional polaronic ground state in superconducting $LiTi_2O_4$

Zubia Hasan,[1,*] Grace A. Pan,[1,*] Harrison LaBollita,[2] Austin Kaczmarek,[3] Suk Hyun Sung,[4] Shekhar Sharma,[2] Purnima P. Balakrishnan,[5] Edward Mercer,[6,7] Vivek Bhartiya,[8] Zaher Salman,[9] Thomas Prokscha,[9] Andreas Suter,[9] Alexander J. Grutter,[5] Mirian Garcia-Fernandez,[10] Ke-Jin Zhou,[10] Jonathan Pelliciari,[8] Valentina Bisogni,[8] Ismail El Baggari,[4] Darrell G. Schlom,[11,12] Matthew R. Barone,[11] Charles M. Brooks,[1] Katja C. Nowack,[3] Antia S. Botana,[2] Brendan D. Faeth,[11] Alberto de la Torre,[6,7,†] and Julia A. Mundy[1,†]

[1]*Department of Physics, Harvard University, Cambridge, MA, USA*

[2]*Department of Physics, Arizona State University, Tempe, AZ, USA*

[3]*Laboratory of Atomic and Solid-State Physics, Cornell University, Ithaca, NY, USA*

[4]*The Rowland Institute, Harvard University, Cambridge, MA, USA*

[5]*NIST Center for Neutron Research, National Institute for Standards and Technology, Gaithersburg, MD, USA*

[6]*Department of Physics, Northeastern University, Boston, MA, 02115, USA*

[7]*Quantum Materials and Sensing Institute, Northeastern University, Burlington, MA, 01803 USA*

[8]*National Synchrotron Light Source II, Brookhaven National Laboratory, Upton, NY 11973, USA*

[9]*PSI center for Neutron and Muon Sciences, 5232 Villigen PSI, Switzerland*

[10]*Diamond Light Source, Harwell Campus, Didcot OX11 0DE, UK.*

[11]*Platform for the Accelerated Realization, Analysis, and Discovery of Interface Materials (PARADIM), Cornell University, Ithaca, NY, USA*

[12]*Department of Materials Science and Engineering, Cornell University, Ithaca, New York 14853, USA*

(Dated: December 5, 2025)

* These authors contributed equally to this work.
† Correspondence should be addressed to: a.delatorreduran@northeastern.edu; mundy@fas.harvard.edu

CONTENTS

S1. SUPPLEMENTARY NOTE 1: SYNTHESIS AND STRUCTURAL CHARACTERIZATION

We used reactive oxide molecular-beam epitaxy (Veeco GEN 10) to synthesize thin film $LiTi_2O_4$ on untreated $MgAl_2O_4$ (111) substrates (CrysTec GmbH). The lithium and titanium fluxes were matched and set to $\sim 1.5 \times 10^{13}$ atoms/cm^2·s as measured by a quartz crystal microbalance (QCM). A titanium molecular beam was generated using a Ti-ball™[1,2]. We obtained the lithium flux by flowing O_2 during the QCM process and forming Li_2O, as the low atomic mass of elemental lithium yields a small frequency change on the QCM below the detection sensitivity except for at very high fluxes. For the deposition process, we heated the substrates with a 10.6 μm CO_2 laser (Epiray GmbH)[3] to 825 °C in a pressure of 1.0 - 2.0 $\times$ 10^{-7} Torr molecular O_2 over a chamber background pressure of $\sim 5.0 \times 10^{-8}$ Torr. We co-deposited the lithium and titanium sources for one hour. After deposition, we shut off the O_2 flow to prevent oxidation of titanium to the 4+ state and cooled at a rate of 100°C/min.

X-ray diffraction confirms the bulk crystallinity of the $LiTi_2O_4$ thin films (Fig. S1(a)). *In-situ* reflection high-energy electron diffraction (RHEED) (Fig. S1b) indicates a smooth surface. Reciprocal space mapping around the 351 peaks of the $MgAl_2O_4$ and $LiTi_2O_4$ indicate that the film is fully relaxed (Fig. S1(c)). From the x-ray diffraction pattern and reciprocal space map, we extract lattice constants of $a = b = c = 8.40 \pm 0.03$ Å. We also rotated our sample in-plane while aligned to the 440 peak as shown in the ϕ scan in Fig. S1c. We expect to see three different peaks for the 440 peak as we rotate in ϕ as shown by the substrate. Surprisingly, our film shows six-fold symmetry with a clear preference for the orientation that is separated 60 degrees from the substrate. This can be seen in Fig. S1c where the sharp film peaks contrast the broad peaks of lower intensity that match the substrate peaks. This has also been observed by[4] and can be seen in the six-fold symmetry of our ARPES Fermi surface (Supp. Mat. Sec S4). We note that the minority phase of the film growing in a rotated domain does not affect the intrinsic physical properties of the film, as demonstrated by the sharp superconducting transitions and high RRR values (Fig. S3).

We note that this is the first time that $LiTi_2O_4$ thin films have been synthesized by MBE; previous films have been synthesized using pulsed-laser deposition (PLD)[5–8]. Typically, pure elemental sources are used for evaporating the constituent elements in a compound. Meanwhile, compounds containing alkali metals are rarely synthesized via MBE due to the pyrophoricity and reactivity of pure alkali sources. Here, we use an intermetallic alloy of lithium and tin with an approximate composition of $Li_{0.2}Sn_{0.8}$. This alloy, which we prepare in a glove box, stabilizes the elemental lithium in air and enables safe, relatively inert loading of the combined source into the MBE. Because tin has a vapor pressure about eight orders of magnitude lower than lithium at the source temperatures used[9], we expect negligible tin evaporation at the operation temperatures of the effusion cell, ~650-675 °C, which produces a lithium flux of $\sim 1.5 \times 10^{13}$ atoms/cm^2*s. This method of stabilizing alkali metals in

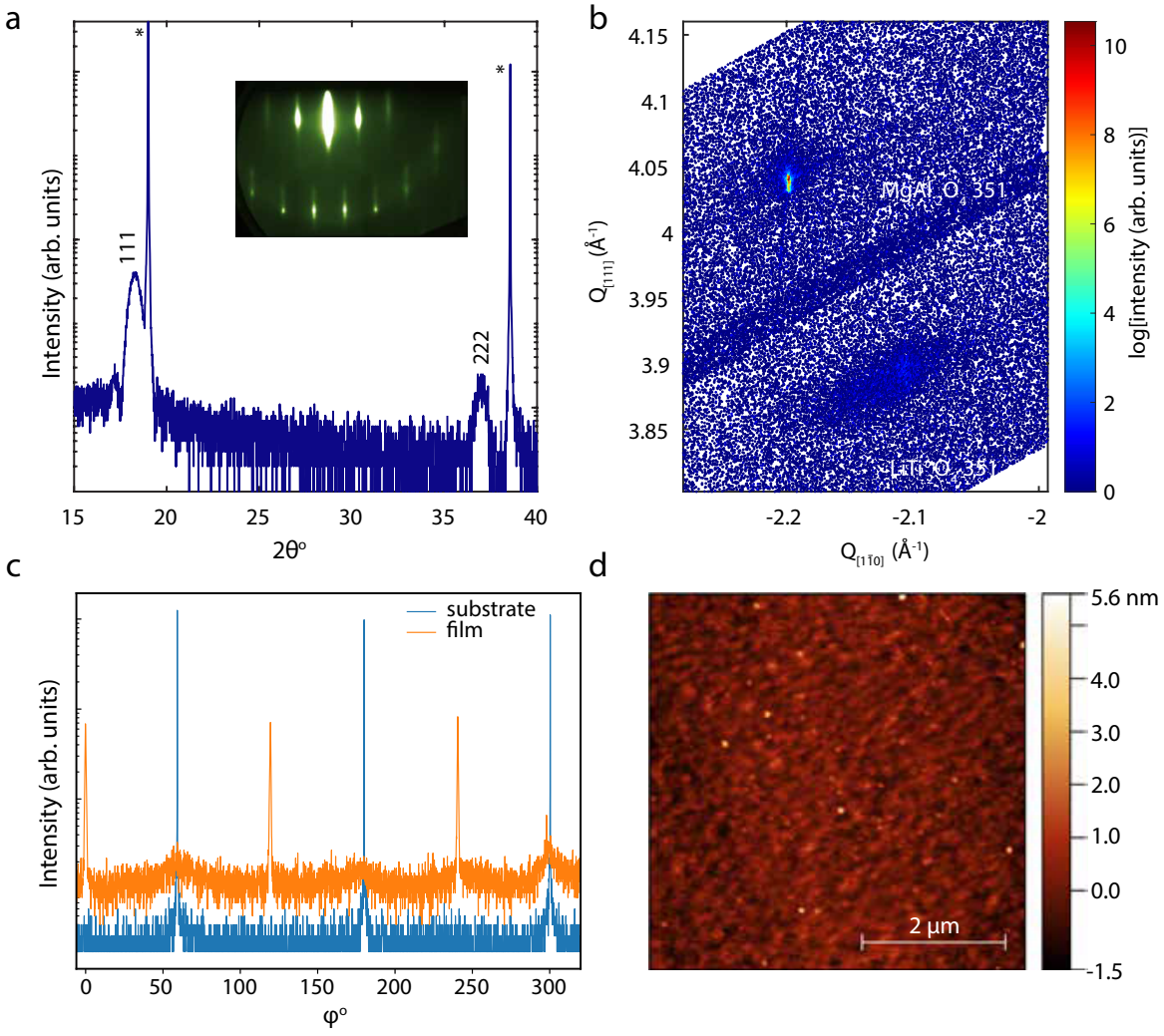

FIG. S1. Structural characterization of a $LiTi_2O_4$ thin film on $MgAl_2O_4$ (111) substrate. (a) X-ray diffraction of $LiTi_2O_4$ film. Asterisks indicate substrate peaks. Inset shows reflection high-energy electron diffraction (RHEED) image along the $[11\bar{2}]$ direction showing a pristine surface after growth and just before transferring to the ARPES chamber. (b) Reciprocal space mapping around the 351 substrate and film peaks. (c) Phi scan around the [440] peak for the substrate (blue) and film (orange), showing three-fold symmetry for the substrate and six-fold symmetry for the film. (d) Atomic force microscope (AFM) image of a sample surface after exposure to air. The root-mean-square roughness is less than 5 Å.

.

intermetallic form for MBE deposition has recently been successfully employed by Ref.[10]

S2. SUPPLEMENTARY NOTE 2: SUPERCONDUCTING TRANSPORT CHARACTERISTICS

We performed all electrical transport measurements in a Hall bar geometry using evaporated Cr/Au (7 nm/100 nm) contacts with the Hall channel defined by a diamond scribe along the $[11\bar{2}]$ crystallographic direction of the $MgAl_2O_4$ (111) substrate. We loaded the samples in a 9 T Dynacool Physical Property Measurement System (PPMS) and used AC lock-in techniques at $\sim$ 15 Hz. In addition to the bulk-like superconducting transition, we observe Fermi-liquid-like ($\rho \sim T^2$) behavior from 20 K - 140 K and a residual resistivity ratio (RRR) of $\sim$6 (Supp Fig. S3a), comparable to the best observed[11] attesting to the high quality of the films.

To estimate the carrier densities of the $\sim$15 nm thick $LiTi_2O_4$ on $MgAl_2O_4$, we measured the transverse resistance R_{xy}, anti-symmeterized the raw data to eliminate the parasitic longitudinal component, and used the Hall relation $R_H = 1/ne$. Figure S2 shows the extracted R_H (a) and n (b) from the anti-symmeterized data. We find that the sign of the carriers for multiple samples is negative, suggesting dominant electron-like carriers, in contrast to what has been established in bulk crystals and thicker films. This agrees with our ARPES observations, which reveals dominant electron-like bands at E_F. We postulate that the proximity of the Lifshitz transition to E_F could be responsible for varying reports of the sign of R_H in separate $LiTi_2O_4$ samples. It is further possible that by bringing $LiTi_2O_4$ down to the thin film limit, as discussed below and in the main text, the system passes through this transition.

Bulk $LiTi_2O_4$ is a three-dimensional (3-D) superconductor with an isotropic response of the superconducting transition to a magnetic field. Our work, which represents the first realization of MBE thin films, brings $LiTi_2O_4$ down to a two-dimensional (2-D) thin film

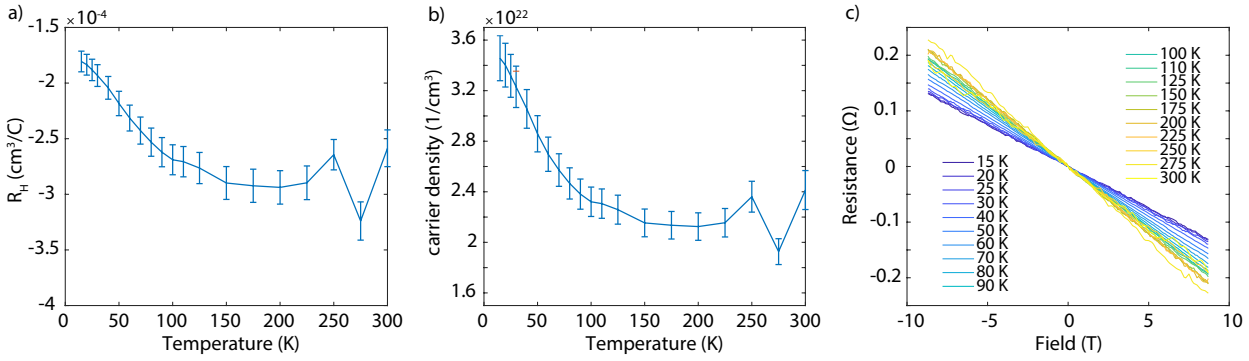

FIG. S2. Hall coefficients R_H (a) and carrier densities (b) of a $LiTi_2O_4$ (111) thin film with anti-symmeterized 'raw' data (c). While the magnitude and lack of substantial temperature dependence R_H is in agreement with bulk and thicker film data, we obtain a negative R_H in multiple films, suggesting a dominant electron carrier-type.

limit and generates a large anisotropy in the critical field ($H_{c2,||}$ and $H_{c2,\perp}$) as well as an enhancement of $H_{c,||}$ close to the Pauli limit. The anisotropy of the critical field reflects the 2-D geometrical confinement of the orbital motion in the in-plane direction. No mass anisotropy leading to critical field anisotropy is expected in bulk $LiTi_2O_4$, suggesting that our (111) oriented thin films sit at the 2-D thin film limit of superconductivity (Supp. Fig. S3).

For thin films with $d < \xi_{GL}$ in magnetic fields much smaller than $H_c(T{=}0)$, orbital depairing effects dominate and we can describe the behavior of $H_c(T_c)$ with the linearized Ginzburg-Landau equations:

$$H_{c,\perp}(T) = \frac{\phi_0}{2\pi\xi_{||}^2(0)}\left(1 - \frac{T}{T_c}\right) \tag{S1}$$

$$H_{c,||}(T) = \frac{\phi_0\sqrt{3}}{\pi\xi_{||}d}\sqrt{1 - \frac{T}{T_c}}\ , \tag{S2}$$

where $H_{c,\perp}$ and $H_{c,||}$ are the $H_c(T)$s out-of-plane and in-plane, respectively, of the film; ϕ_0 is the superconducting magnetic flux quantum $h/2e$, $\xi_{||}$ is the in-plane Ginzburg-Landau coherence length, and d is the superconducting film thickness. From these equations, we extract $\xi_{||} = 3.37 \pm 0.03$ nm and $d = 12.1 \pm 0.3$ nm (Fig. S3(b)), close to the full thickness of the film as determined from growth rates and times during MBE synthesis. (All T_c's are determined by the midpoint of the resistive transition, i.e. $T_c^{50\%}$.) We can further use the carrier concentrations from Hall measurements (Supp Fig. S2) to estimate a mean free path $l_0 \approx 1.01$ nm from a Drude model approximation of $l_0 = \hbar(3\pi)^{2/3}/(e^2n^{2/3}\rho_0)$, placing our $LiTi_2O_4$ thin films in the dirty limit of superconductivity where $l_0 < \xi$. In this limit, we calculate a BCS coherence length from $\xi = 0.855\big(\xi_{\rm BCS}l_0/(1 - \frac{T}{T_c})\big)^{1/2}$ of $\xi_{\rm BCS} \approx 15.4$ nm. With this simplified Drude model picture, we can provide a crude approximation of the expected BCS superconducting gap. We use the Fermi velocity ν_F of the principal band at the Fermi level E_F (Fig. S7(a)) to estimate from $\xi_{\rm BCS} = \hbar\nu_F/\pi\Delta$ that Δ lies between 1.45 meV and 2.07 meV. This is coincident with the gap size extracted from fits to the temperature-dependent penetration depth taken using scanning SQUID in Section S3.

While an exact application of Eqs. S1 and S2 is strictly valid only in the limit where $d < \xi$, we note that corrections to $H_{c,||}$ are on the order of only a few percent in the regime where $d \sim 2\xi$. We can verify a potential two-dimensional (2-D) geometrical confinement scenario using the functional dependence of T_c on the angle θ between the magnetic field and the sample. Tinkham[12] showed that the angular dependence of the critical field of a thin film can be expressed as

$$\left(\frac{H_c(\theta)\ \sin\theta}{H_{c,||}}\right)^2 + \left|\frac{H_c(\theta)\ \cos\theta}{H_{c,\perp}}\right| = 1\ , \tag{S3}$$

where here the angle θ is between the field and the sample normal, i.e., $\theta = 0$ is out-of-plane of the sample, and $H_{c,||}$ and $H_{c,\perp}$ are the zero-temperature critical fields. This implicit expression in $H_c(\theta)$ can be re-arranged using Eqs. S1, S2 to write T_c as a function of θ:[13]

$$\frac{T_{c2}(\theta)}{T_{c0}} = 1 - \left|\left(1 - \frac{T_{c2}^{\perp}}{T_{c0}}\right)\cos\theta\right| - \left(1 - \frac{T_{c2}^{||}}{T_{c0}}\right)\sin^2\theta \,, \tag{S4}$$

where now T_{c0} represents the zero-field critical temperature and $T_{c2}^{\perp}$ and $T_{c2}^{||}$ are the finite-field critical temperatures. This functional form yields a distinctive cusp around $\theta = 90°$, reflecting the sensitivity of the critical temperature to small out-of-plane field components.

An alternative explanation for the observed superconducting anisotropy is the 3-D generalization of Ginzburg-Landau theory. In this scenario, the effective masses can vary substantially along crystallographic directions, affecting the orbital electron motion and hence the critical fields. This anisotropy is related via the expression $m_{||}^*/m_{\perp}^* = H_c^{\perp}/H_c^{||}$ and can be captured generally with the equation:

$$H_c(\theta) = H_c^{\perp}\left(\cos^2(\theta) + \frac{m_{||}}{m_{\perp}}\sin^2(\theta)\right)^{-1/2} . \tag{S5}$$

As before, this can be rewritten as a function of T_c instead:[13]

$$T_{c2}(\theta) = T_{c0} + H_0\frac{\partial H_c^{\perp}}{\partial T}\left(\cos^2\theta + \frac{m_{||}}{m_{\perp}}\sin^2\theta\right)^{1/2} \tag{S6}$$

Comparing the 2-D Tinkham model and the 3-D anisotropic Ginzburg-Landau model, we observe that the 2-D Tinkham model better captures the behavior of the experimental $T_{c2}(\theta)$, especially around the cusp near $\theta = 90°$ (Fig. S3(c)). Importantly, while the 3-D anisotropic Ginzburg-Landau model appears to also produce a similar cusp-like behavior around $\theta = 90°$, this is only in the unphysical limit where $m_{||}^*/m_{\perp}^* \to 0$. Extraction of m^* using angle-resolved photoemission, either from analysis of Fermi pocket sizes or from comparing experimentally renormalized bands with bare DFT-calculated bands, in Sec. S4 indicates that $m^* = 2.53m_e \pm 0.6$, indicating that there is no strong mass anisotropy in $LiTi_2O_4$. Hence, we conclude that our ~12 nm thin film $LiTi_2O_4$ on $MgAl_2O_4$ represents the first explicit realization of superconducting $LiTi_2O_4$ in the 2-D thin film limit, as other studies observe superconductivity only in films thicker than ~30 nm[5–7].

In this limit, orbital depairing is suppressed and generates a large enhancement of $H_{c,||}$. Here, this $H_{c,||}$ approaches or potentially exceeds the Pauli limit $H_P = 1.86(T/K) * T_{c0}$, as suggested by the Ginzburg-Landau fits (Fig. S3(c)). We consider that in addition to orbital depairing, paramagnetic depairing effects may also contribute to the behavior of H_c: while Eq. S2 apparently fits the data well, paramagnetic effects can also give rise to a $(1 - T/T_c)^{1/2}$ functional dependence of H_c[14]. In a system where spin-independent transport

scattering dominates over spin-orbit scattering (a probable scenario since $LiTi_2O_4$ is a dirty limit superconductor, as discussed above), we can generally describe the behavior of H_c using Werthamer-Helfand-Hohenberg (WHH) theory[15]. The WHH model containing only orbital effects is written as:

$$\ln\left(\frac{1}{t}\right) = \psi\left(\frac{1}{2} + \frac{\bar{h}}{2t}\right) - \psi\left(\frac{1}{2}\right) \tag{S7}$$

where $t = T/T_c$ and $\bar{h} = 2eHv_F^2\tau/6\pi ck_BT_c$ are fitting parameters and ψ is the digamma function. This orbital WHH model well-captures the behavior of $H_{c,\perp}(T)$ but fails to converge for $H_{c,||}(T)$ (Fig. S3(b)), indicating a substantial presence of paramagnetic and/or spin-orbit interaction effects in $LiTi_2O_4$. The paramagnetic and spin-orbit interaction effects are represented in the full WHH model[15], although we do not attempt to fit the full WHH model to $H_{c,||}(T)$. Due to the sensitivity of the full WHH model to H_c close to $H_c(T{=}0)$, our current $H_{c,||}(T)$ data severely underconstrains the WHH fit, making the extraction of the Maki parameter α (paramagnetic contribution) and spin-orbit interaction λ_{SO} unreliable. Higher-field data could help clarify these interaction terms, though such an effort is beyond the scope of the present study. Nevertheless, our current work suggests that $LiTi_2O_4$ in the 2-D thin film limit reveals a $H_{c,||}(T)$ that appears to approach or exceed the Pauli limit and potentially harbors strong paramagnetic or spin-orbit interaction effects.

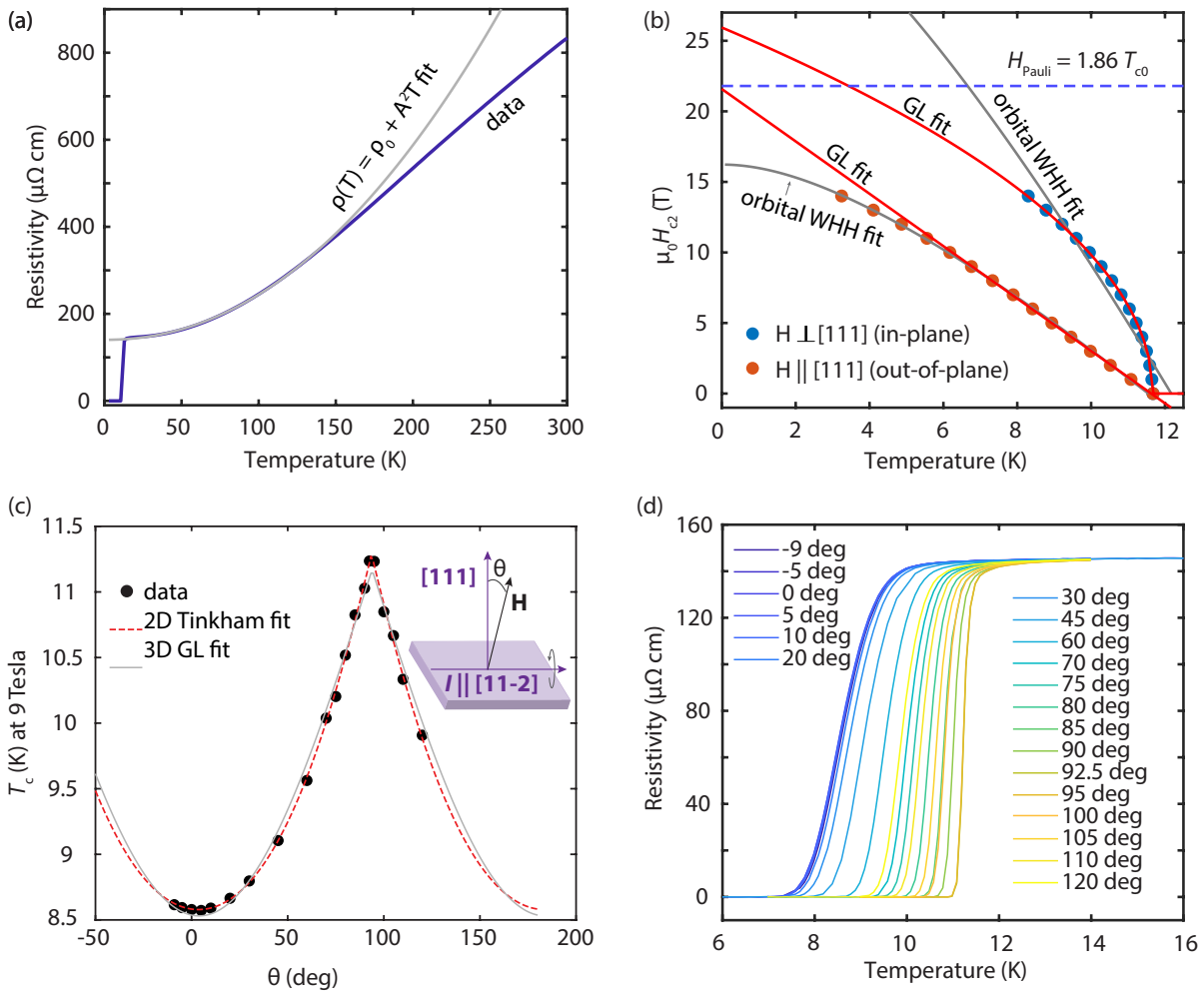

FIG. S3. Superconducting transport characterization. (a) Full resistivity curve of $LiTi_2O_4$. A $\rho \sim T^2$ Fermi-liquid dependence is observed in range 15 - 140 K. (b) Variation of the critical field H_c with temperature. Red lines, Ginzburg-Landau fits. Grey lines, WHH fits considering only orbital effects. Blue dashed line, Pauli limit. (c) Dependence of the critical temperature on the angle that a 9 Tesla magnetic field makes with the sample normal. (d) The superconducting transitions at various sample angles used to create the plot in c.

S3. SUPPLEMENTARY NOTE 3: LOCAL MAGNETIC MEASUREMENTS USING SCANNING SQUID MICROSCOPY

We use scanning SQUID susceptometry to measure the temperature dependence and spatial variation of the diamagnetic response in the sample. We additionally image magnetic features such as superconducting vortices. The scanning SQUID susceptometer consists of a pickup coil and a concentric field coil with inner radius 0.75 μm and 3.0 μm and outer radius 1.6 μm and 6.0 μm, respectively[16]. An ac-current at a frequency of approximately

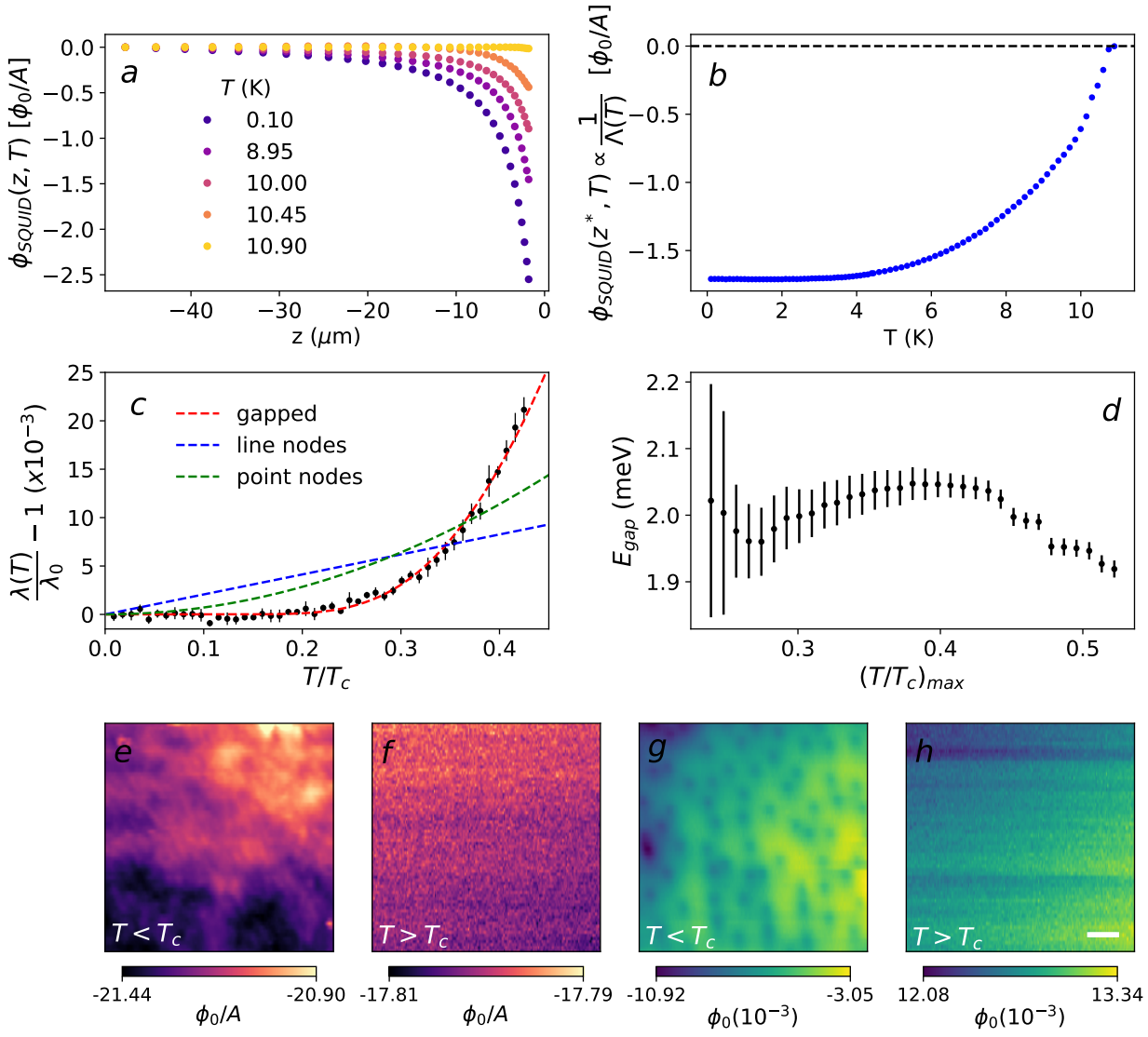

FIG. S4. (a) The change in mutual inductance between the field and pickup coil as a function of the SQUID-sample distance z for select temperatures. (b) Temperature dependence of the mutual inductance at fixed height $z^* = 3$ μm, directly proportional to the inverse Pearl length. (c) Temperature dependence of the reduced penetration depth showing attempted fits based on line nodes and point nodes in the superconducting order parameter. (d) Variation of the extracted gap energy with the upper bound of the temperature range used for fitting. (e) Image of the diamagnetic response in the superconducting phase at $T = 9$ K. (f) Image of the magnetic response above T_c revealing the absence of spatial structure. (g) Image of the static magnetic flux above the sample acquired at $T = 4$ K after cooling in a small field. A number of vortices are visible in the field of view. (h) Image of the static magnetic flux above T_c showing the absence of magnetic structure within our spatial resolution of a few micrometer. Scale bar = 20 μm applies to (e-h).

200 Hz in the field coil generates a small magnetic field, and we measure the resulting flux in the pickup coil using a lock-in amplifier. Far from the sample surface, we measure the mutual inductance between the pickup and field coils. When the pickup / field coil pair approaches the sample, the magnetic susceptibility of the sample appears as a change in the mutual inductance. Above T_c, approaching the sample surface shows no change in mutual inductance within our noise floor (yellow data in Fig. S4(a)). Below T_c, as we approach the sample surface, the screening currents of the sample in the superconducting state reduce the local field applied by the field coil, and we observe a reduction in the mutual inductance between the two coils. The strength of the screening currents can be directly related to the 2-D Pearl length of the thin film[17].

We measure the temperature dependence of the diamagnetic response by recording the mutual inductance as we gradually approach the SQUID to the sample surface at fixed temperature values. To vary the temperature of the sample, we thermally connect the sample only weakly to the fridge and control its temperature using a heater and thermometer close to the sample. In this way, we can change the sample temperature from 100 mK to 12 K while the temperature of the mixing chamber plate of the dilution refrigerator and the SQUID varies only between 20 mK and 260 mK. Our data, therefore, consists of the temperature and height-dependent mutual inductance $\phi(z, T)$, which we report in units of ϕ_0/A with ϕ_0 the flux quantum. Approach curves at select temperatures are shown in Fig. S4(a). An offset has been subtracted at the largest distance between the sample and SQUID, which corresponds to the unperturbed mutual inductance between the pickup and field coil. In addition, the measured flux is divided by the current applied to the field coil, which was 1.4 mA for this measurement. The approach curves can be modeled by $\phi(z, T) = F(z)/\Lambda(T)$ where $\Lambda(T)$ is the temperature-dependent 2-D Pearl length, and $F(z)$ is a function of the SQUID-sample distance z and several other geometrical properties of the measurement[17]. Importantly, this implies that at a fixed distance $z = z^*$, changes with temperature in $\phi(z^*, T)$ are only a result of changes in the inverse of the 2-D Pearl length, which approaches 0 as T approaches T_c. In Fig. S4(b) we show $\phi(z^*, T)$ for $z^* \approx -3$ μm extracted from a set of approach curves. The temperature at which the signal exceeds our noise floor is 11.3 K, which we use as T_c in the discussion of the SQUID data. At low temperature, we observe that the mutual inductance saturates. We therefore assume that the signal at the lowest temperatures ($T < 1$ K) reflects the signal level for $\Lambda_0 = \Lambda(T = 0)$. This allows us to extract the Pearl length normalized to its low temperature value, $\Lambda(T)/\Lambda_0$, from $\phi(z^*, T)/\phi(z^*, T < 1K)$ independent of z^* and $F(z)$, i.e. all geometric factors cancel.

From the normalized Pearl length, we can determine the reduced London penetration depth $\frac{\lambda(T)}{\lambda_0} - 1$, where λ is the penetration depth and $\lambda_0 = \lambda(T = 0)$. The London penetration depth λ is related to the 2-D Pearl length Λ by $\lambda = \sqrt{\frac{t\Lambda}{2}}$ where t is the film thickness. Therefore, $\frac{\lambda(T)}{\lambda_0} = \sqrt{\frac{\Lambda(T)}{\Lambda_0}} = \sqrt{\frac{\phi(z^*,T_0)}{\phi(z^*,T)}}$. The reduced penetration depth $\frac{\lambda(T)}{\lambda_0} - 1$ is plotted as a function of temperature in Fig. S4(c). The data points shown are averages of values

obtained between $z* = -3$ and $-6\mu m$. The error bars correspond to the standard deviation of these values.

We fit the reduced penetration depth to a fully-gapped model of the form $\frac{\lambda(T)}{\lambda_0} - 1 = \sqrt{\pi\Delta/2k_BT}\ \exp(-\Delta/k_BT)$[18]. The resulting superconducting gap, Δ, has a weak dependence on the highest temperature that is included in the fit, which we report in units of T_c, i.e. $(T/T_c)_{max}$. We extract a Δ ranging from 1.98 meV to 2.05 meV for $0.3 < (T/T_c)_{max} < 0.45$. Fig. S4(c) shows a fit for $(T/T_c)_{max} = 0.425$. In Fig. S4(d), we show the result for the extracted gap as a function of $(T/T_c)_{max}$. If $(T/T_c)_{max}$ is too low, then the fit is dominated by the flat part of the curve in which the measurement errors lead to a large uncertainty in the fit. If $(T/T_c)_{max}$ is too large, the temperature dependence of the gap becomes important. In Fig. S4(c), we additionally show fits corresponding to superconducting order parameters with line nodes and point nodes which would show T and T^2 dependence of the reduced penetration depth respectively[19], neither of which are consistent with the data.

In addition, we image the diamagnetism in the superconducting phase as shown in Fig. S4(e). We observe spatial structure of the diamagnetism both on a larger scale of several tens of μm shown by the bright and dark patches and on a smaller scale of a few μm visible as filament-like structure. This diamagnetic structure is absent above T_c shown in Fig. S4(f) verifying it is a feature of the superconducting phase. The details of this spatial structure is left to future study. We also image static magnetic structure in the sample by measuring the total flux passing through the SQUID pickup coil. Fig. S4(g) shows vortices in the sample when it is cooled in a small field. We used the absence of vortices in our field of view as an indication of a zero-field-cooled state. Above T_c, Fig. S4(h) shows no sign of magnetic features within our spatial resolution of a few micrometers.

S4. SUPPLEMENTARY NOTE 4: ANGLE-RESOLVED PHOTOEMISSION SPECTROSCOPY

ARPES measurements were taken with a Scienta Omicron DA30-L electron analyzer equipped with a Fermion Instruments BL1200s multi-gas discharge lamp using He-I photons at 21.2 eV, Ne-I photons at 16.85 eV, and He-II photons at 40.8 eV (Fig. S5). Measurements were taken by immediately transferring the samples through an ultrahigh vacuum manifold (pressure $< 2 \times 10^{-9}$ Torr) to a measurement chamber (pressure $\sim 5 \times 10^{-11}$ Torr) immediately following film growth. Data collected using Ne-I was processed after acquisition to remove doublet emission features using a method described elsewhere[20]. The base pressure in the ARPES system is maintained during measurements at pressures lower than 5×10^{-11} Torr. ARPES measurements were at a temperature of 7 K and at a nominal experimental energy resolution of 10 meV unless otherwise indicated.

To avoid sample charging during ARPES measurements, films were grounded using a retractable contact pin built onto the sample manipulator. Films were confirmed to be superconducting during low-temperature ARPES measurements by simultaneous *in situ* resistivity measurements performed using these same grounding contact pins. For all measurements, the Fermi level is referenced to the measured Fermi edge of a metal post in direct electrical contact to the sample. No superconducting energy gap was clearly evident, likely owing to the limited experimental energy resolution ($\sim$10 meV) compared to the anticipated gap magnitude ($\sim$1 meV at 8K).

The out-of-plane momentum k_z sampled by ARPES measurements at multiple photon energies was determined based on comparisons of the measured Fermi surface contours and energy-momentum dispersions against density functional theory calculations. Approximating the photoemission process with a free electron final-state model, the measured out of plane momentum k_z can be written as

$$k_z = \sqrt{(2m_e/\hbar^2)\,(V_0 + E_k) - k_{\|}^2}, \tag{S8}$$

where m_e is the electron mass, E_k is the outgoing electron kinetic energy, $k_{\|}$ is the total in-plane momentum (determined from E_k and the emission angle) and V_0 is the inner potential. Taking V_0 to be 9 eV and $k_{\|}$ to be 0.65 Å^{-1} (the relevant in-plane momentum for features of interest near the surface BZ boundary) results in k_z values of -0.06, -0.3, and -0.49 Å^{-1} relative to the 3D BZ center (Γ) for He-Iα, Ne-Iα, and He-IIα photons, respectively. These values produce broadly self-consistent results and good agreement between observed spectral features and DFT-derived bandstructure, as demonstrated in the main text and in Fig. S5(a).

Fig. S5(a) displays the first Brillioun zone (BZ) for an face-centered cubic (FCC) lattice in the [111] direction, matching the growth geometry of our films. In this orientation, the

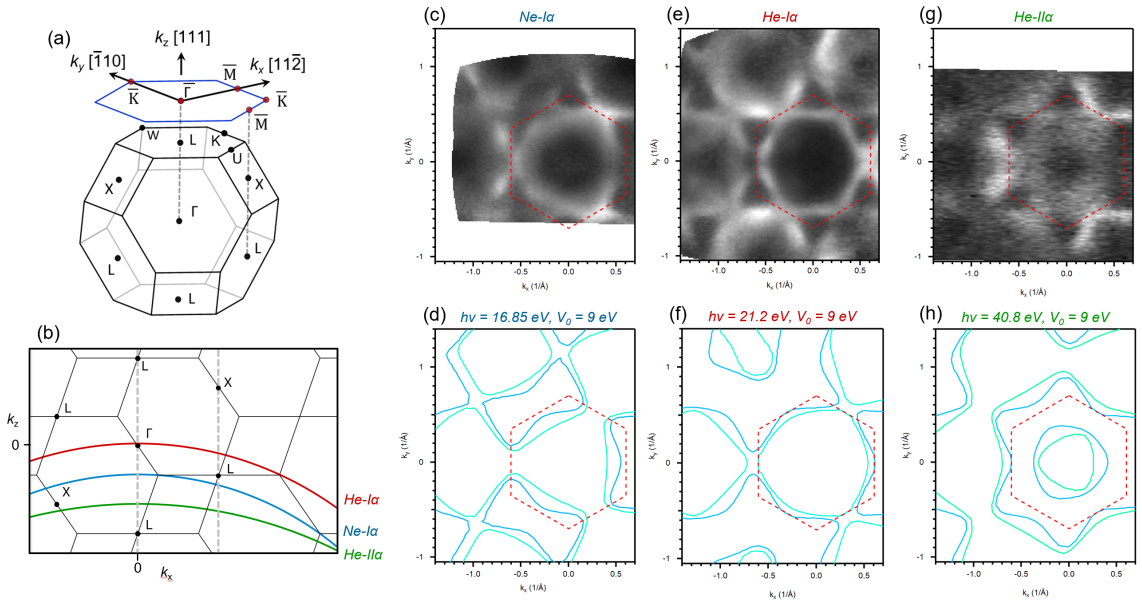

FIG. S5. ARPES measurements on $LiTi_2O_4$ using several plasma lamp photon energies. (a) The bulk fcc Brillouin zone (BZ) of $LiTi_2O_4$ and corresponding 2D surface BZ (blue). (b) The bulk BZ in the $k_x - k_z$ plane as viewed along the k_y direction. Solid lines indicate the k_z dispersion for measured cuts using He-Iα (21.2 eV), Ne-Iα (16.85 eV), and He-IIα (40.8 eV) light (red, blue, and green respectively). (c), (e), and (f) show iso-energy photoemission intensity maps taken at the Fermi level for He-Iα, Ne-Iα, and He-IIα respectively. (d), (f), and (h) show the corresponding DFT-calculated Fermi surfaces corresponding to the momentum sheets in (b) for each photon energy. Good agreement is found when using an inner potential V_0 of 9 eV.

surface brillioun zone (SBZ, blue) is hexagonal, with the surface $\bar{M}$ points corresponding to the projection of the X and L points of the bulk BZ as shown. Note that we define here by convention the in-plane reciprocal lattice vectors k_x and k_y to be parallel with [11$\bar{2}$] and [$\bar{1}$10] directions, respectively. Due to the the distinct three-dimensional structural character of $LiTi_2O_4$, ARPES measurements at different photon energies probe non-equivalent k_z ranges. Fermi surface maps taken with He-Iα, Ne-Iα, and He-IIα photons are shown in Fig. S5. The Ne-Iα, and He-IIα maps (Fig. S5(c) and (g) show distinctly different Fermi surfaces compared to the map taken with He-Iα(Fig. 2c) demonstrating the three-dimensional structural character of $LiTi_2O_4$.

While DFT captures the qualitative features of the Fermi surface for $LiTi_2O_4$ very well, we observe some interesting departures from experiment in some of the given data. For example, DFT captures two degenerate bands, from two in-equivalent titanium sites, populating the Fermi surface. This is in agreement with the calculated band structure, Figure S14a which shows two degenerate Ti-3d bands crossing the Fermi level in the $\bar{\Gamma} - \bar{K}$. While our experimental Fermi surface maps are unable to resolve between the two bands due to

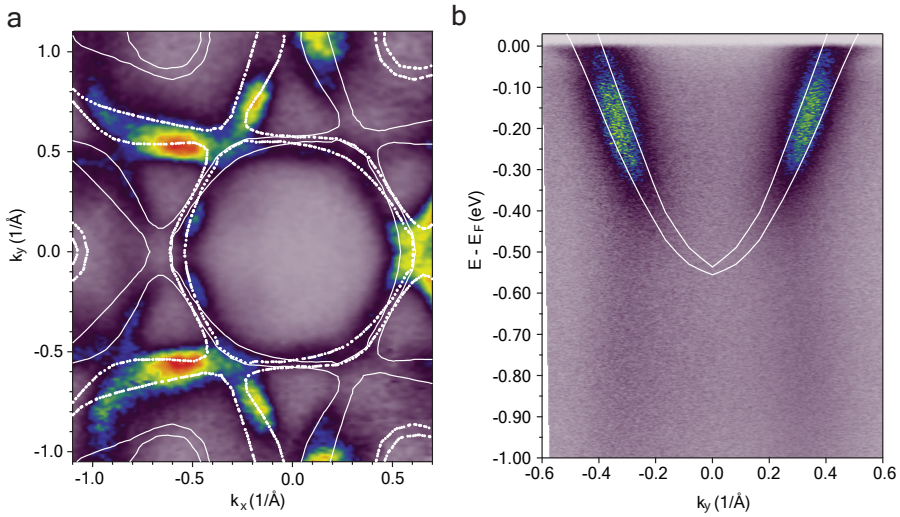

FIG. S6. (a)He-Iα Fermi surface overlaid with DFT calculated Fermi surface. Lines and dots represent two different 180 degree rotated domains. (b) Ne-I data for the $\bar{\Gamma} - \bar{K}$ cut. White lines represent the DFT overlay.

their close proximity, we attribute the broadening in the Ne-Iα data (Fig. S6b) to two unresolved bands present at this k_z. Furthermore, we note that the spectral intensity at 1 eV binding energy near the zone center highlighted in the main text (Fig. 2d) disappears in the Ne-I data along the same cut in momentum space. However, two distinct waterfall features can be seen in the Ne-I data (Fig. S6b), interpreted as a signature of strong correlations.

Our ARPES measurements of this material display a hexagonal, electron-like Fermi contour within the first surface Brillouin zone overlaid with density functional theory (DFT) calculations (Fig. S6a). We notice that the hexagonal symmetry of the Fermi surface is contrary to the overlaid three-fold symmetry calculated via DFT; we observe this via our phi scans where we see an additional three-fold symmetry superimposed over the three-fold symmetric spinel substrate(Fig. S1). Moreover, $LiTi_2O_4$ is reported to grow in 180 degree rotated domains[4] which would create a superimposed Fermi surface of two domains with different orientations. $LiTi_2O_4$ displays a distinct band structure where electron pockets push against the boundaries of the first Brillouin zone in proximity to a Lifshitz transition. Often, Fermi surface reconstructions result in dramatic changes in magnetoresistive behavior[21,22], therefore proximity to such a transition could explain anomalous magnetotransport in $LiTi_2O_4$[23].

Temperature and Momentum dependence of kink structure

The presence of electron-phonon coupling (EPC) in $LiTi_2O_4$ can be shown by the electron self-energy, shown in S7 (b), where the lineshapes of Σ' and Σ'' are consistent with simple Debye-like coupling to a phonon mode. Here, Σ' is obtained by subtracting the estimated effective bare band from the measured renormalized band energy, whereas Σ' is determined

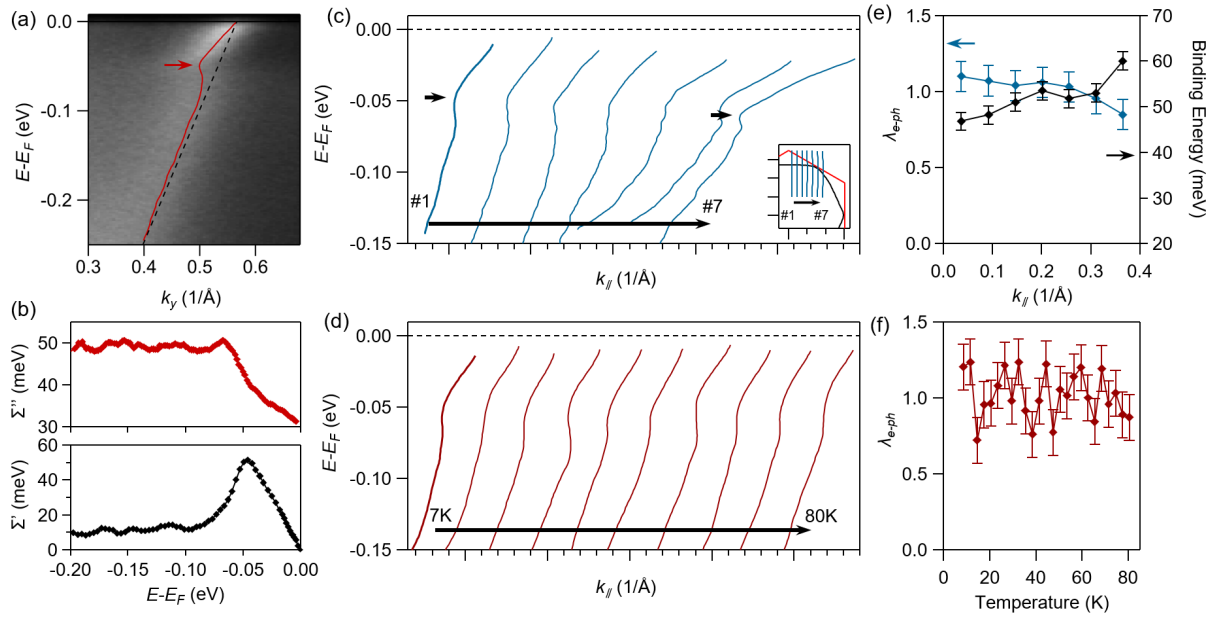

FIG. S7. Evolution of kink behavior with momentum and temperature. (a) The outline of the kink overlaid with a fit to the extracted MDC points (red line). The black dotted line shows the bare band fitted to the MDC at lower binding energy. (b) The real and imaginary part of the electron self-energy clearly showing a peak where the kink is present in momentum space. The momentum dispersion of the MDCs is shown in (c) with the inset corresponding to the cuts taken for each MDC curve. λ_{e-ph} shows a decreasing trend as we move away from Γ, highlighted in (e). Evolution of the kink with temperature is shown in (d) from 7 K to 80 K, and the extracted values of λ_{e-ph} are displayed in (f), demonstrating a linear trend.

from the fitted MDC half-width at half-maximum multiplied by the bare Fermi velocity[24]. To further explore the electron-phonon coupling, we measure the evolution of the kink above and below T_c from 7 K to 80 K. Interestingly, we observe no change in λ_{e-ph} above and below the superconducting transition. Fig. S7(f) shows little to no deviation in the coupling strength from 7 K to 80 K. This is corroborated by[25] who see no change in the kink until 150 K, after which it disappears. This is also confirmed by temperature-dependent calculations (Supp. Mater. Sec. S5) which show a kink that gradually smooths out by 100 K. λ_{e-ph} is calculated using $\lambda_{e-ph} = \frac{\nu_o}{\nu_f} - 1$ where ν_o is the velocity of the bare band and ν_f is the velocity of the renormalized band. By fitting the dispersion at higher binding energies to ν_f and lower binding energies to ν_o we can extract the EPC. Note that $\lambda_{tot} = 1.8$ reported in the main text has been calculated the same way as described above, but with ν_o extracted from fitting the DFT-calculated bands at $\bar{\Gamma}$ - $\bar{K}$ for higher accuracy. This treatment includes the strength of electron-electron correlations (λ_{e-e}), as well as electron-phonon coupling (λ_{e-ph}). The dispersion of the kink as shown in Fig. S7c, d and Fig.3a is extracted by fitting the position of momentum dispersion curves (MDC) peaks at several binding energies to Lorentzians.

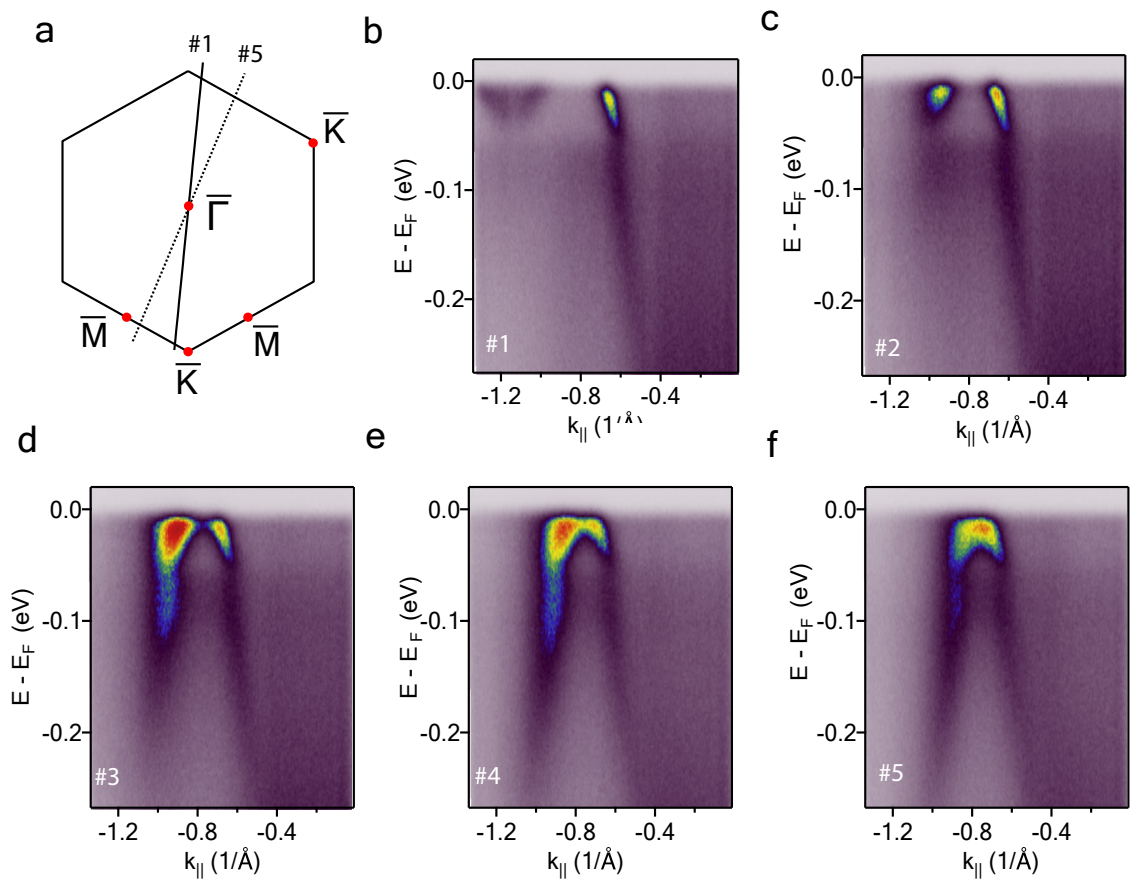

FIG. S8. High statistic cuts of $LiTi_2O_4$ moving from $\bar{\Gamma} - \bar{K}$ to $\bar{\Gamma} - \bar{M}$. (a) The first Brillouin zone of $LiTi_2O_4$. #1 to #5 correspond to cut shown in (b) to (f) respectively, with (c), (d) and (e) spanning between the two cuts.

Calculation of effective mass

The effective mass was calculated by using the following relationship: $m^* = \frac{\hbar^2}{2\pi}\frac{dA_{FS}}{dE}$ where A_{FS} is Fermi surface volume. To extract the Fermi surface volume, we find the area of the iso-energy maps at the Fermi level and at lower binding energies corresponding to the ones shown in Fig. S9a, b and c. By fitting a line of best fit to the iso-energy area maps and their corresponding binding energies with respect to the Fermi level, we are able to find $\frac{dA_{FS}}{dE}$. Using this method we extract $m^* = 2.53 \pm 0.6$ as reported in the main text. We note that using a different method, whereby we fit the band in the $\bar{\Gamma} - \bar{K}$ cut (Fig. 2d) to a simple quadratic function ($E = E_o + \frac{\hbar^2 k^2}{2 * m_e}$) where m_e is the effective mass of the electron and repeat this fit with the bare DFT bands gives a similar result as the effective cyclotron mass. The consistency between both methods demonstrates significant band renormalization due to electron-electron correlations in $LiTi_2O_4$.

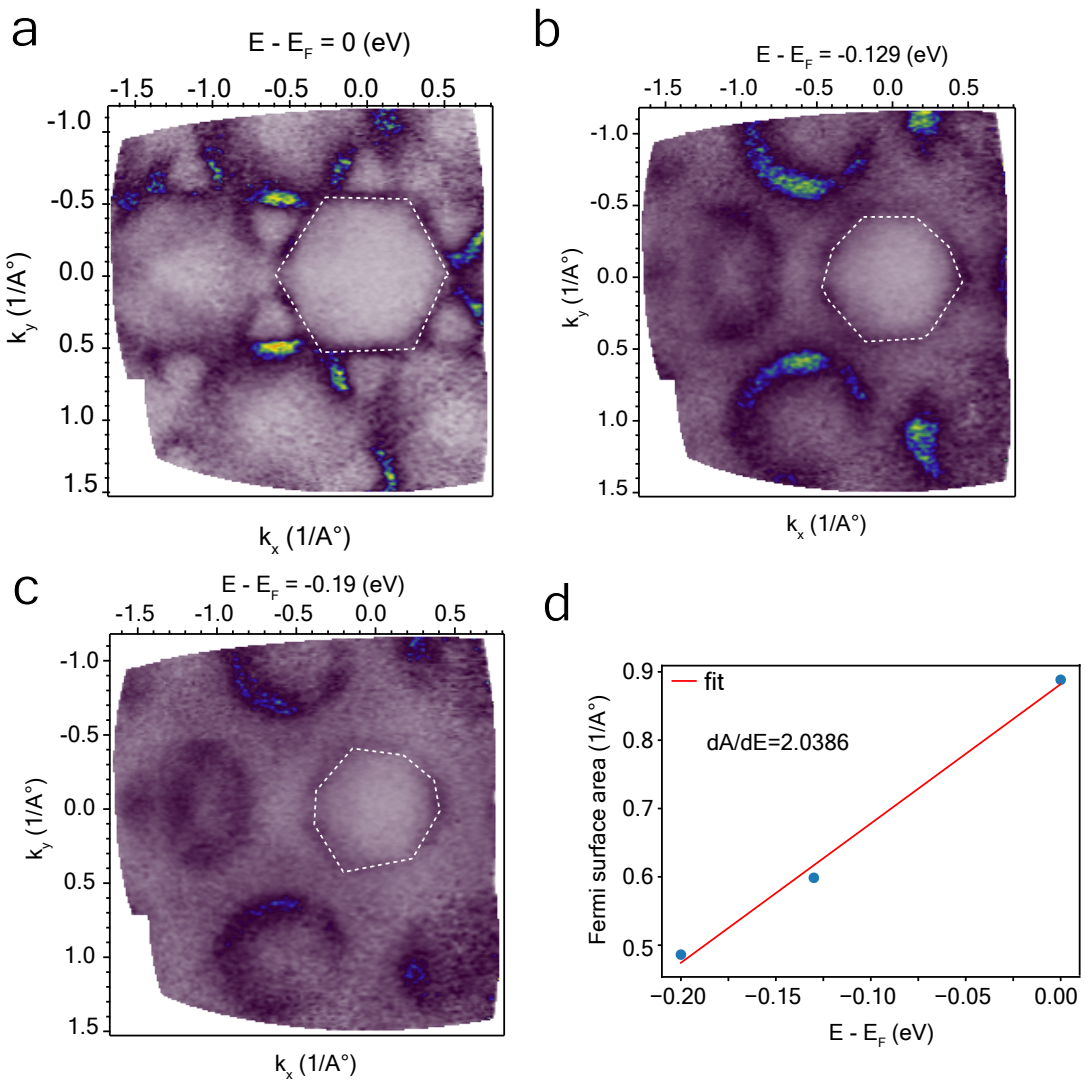

FIG. S9. Cyclotron mass calculation for $LiTi_4O_4$. **a,b,c**, The iso-energy maps of $LiTi_2O_4$ at the Fermi level and lower binding energies respectively. The area of the maps used for the effective mass calculation is highlighted by a white dotted line. **d**, Extracting $\frac{dA}{dE}$ from a linear fit shown via the red line.

Consistency of ARPES spectral features

To establish the consistency of certain ARPES spectral features, we show below ARPES measurements of samples synthesized at different times. We conclude that even if there are un-detectable changes in lithium content that are not captured by our x-ray, RHEED, transport or STEM imaging data, they do not account for spectral features observed in our ARPES data. Figure S10 shows the ARPES band structure of the different samples, all showing incoherent spectral weight that emerges at $E \approx 0.6$ eV, and extends down to $E \approx 0.9$ eV (Fig. 2d) and a dispersionless spectral feature at $E \approx 70$ meV. The consistency in our ARPES data across many different samples indicates that if there are slight deviations

from stoichiometry in our samples that are outside of our measurable range, they do not contribute to the ARPES spectral features discussed above and instead it is likely that these features are due to the intrinsic polaronic nature of $LiTi_2O_4$.

To establish the high crystalline quality and lack of secondary phases of all the samples in Fig. S10, we have included RHEED images of the samples taken right before the *in-situ* transfer to ARPES (Fig. S11). The different growth conditions of the samples are included in the Table S1 below. We note that the high variation in the growth temperature between sample 1 and the other samples is due to the difference in the substrate preparation. Sample 1 was synthesized on a native single-side polished (111)-oriented $MgAl2O_4$ substrate whereas samples 2-4 were synthesized on substrates which previously were backside coated with platinum. These backside coatings were partially removed prior to synthesis but nevertheless these substrates required higher power from the substrate laser heater compared to an uncoated substrate, producing a higher nominal substrate temperature. The variance in the growth temperature of the lithium cell and current/voltage of the Ti-ball™is due to a decrease in flux rate as the source material depletes over the course of several growths. The oxygen pressure is kept constant throughout. Even though the samples were grown at different times, they consistently show high crystallinity and a RHEED pattern that is expected for a homogenous spinel phase, without secondary phases.

Sample	Date	Li cell (°C)	Ti-ball™(A/V)	Growth temperature (°C)	Oxygen pressure (Torr)
1	7/4/2024	660	27.23/20.73	780	2E-2
2	12/8/2022	675	29.8/20.69	825	2E-2
3	12/7/2022	675	29.15/19.99	825	2E-2
4	12/5/2022	675	29/19.92	825	2E-2

TABLE S1. Growth conditions for different samples across two years.

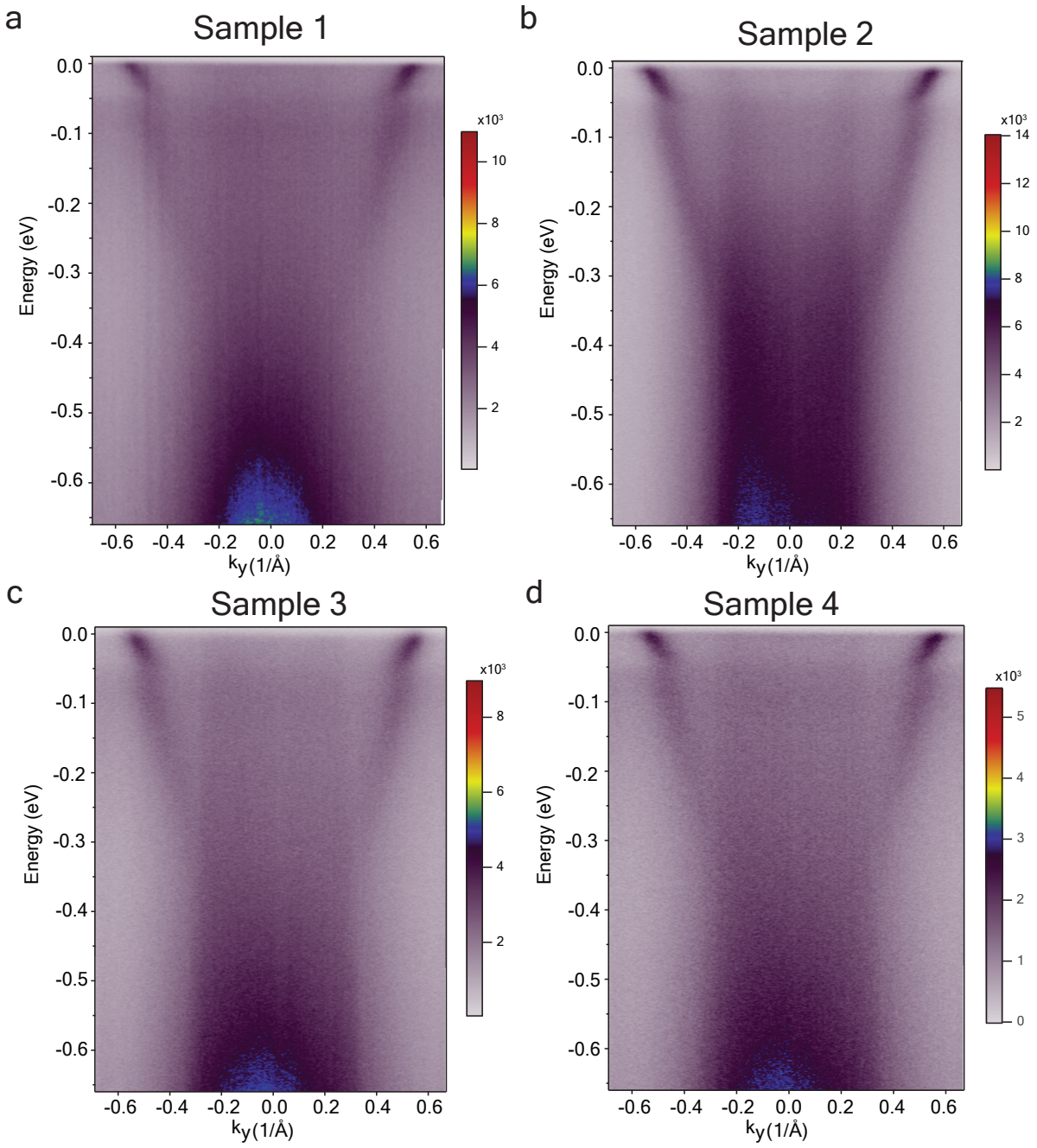

FIG. S10. a-d)ARPES band structure of different samples synthesized over the period of two years. All samples show consistent spectral features like the flat dispersionless feature at $E \approx 70$ meV and the incoherent spectral weight around $E \approx 0.6$ eV extending all the way down to 1 eV (not pictured here but shown in Fig. 2d of the main text).

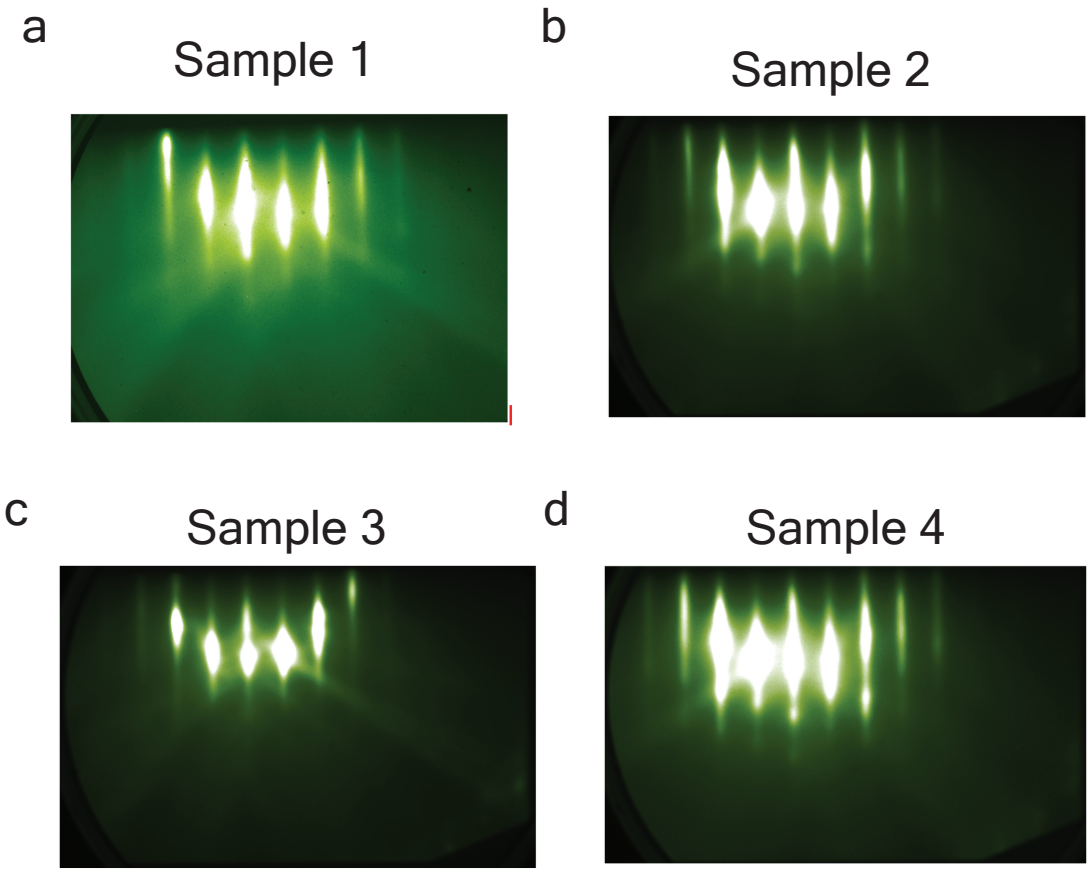

FIG. S11. a-d) RHEED images corresponding to samples in Fig. S10. All images were taken after growth and before *in-situ* transfer to ARPES. All samples show pristine surface quality with no visible secondary phases or signatures of surface reconstruction due to excess or deficient lithium or oxygen.

S5. SUPPLEMENTARY NOTE 5: DFT, DFT+DMFT, AND ELECTRON-PHONON CALCULATIONS. COMPUTATIONAL DETAILS AND ADDITIONAL DATA

Computational details. The spinel-oxide, $LiTi_2O_4$ crystallizes in a face-centered cubic crystal structure belonging to the $Fd\bar{3}m$ (#227) space group. The crystal structure was optimized within density functional theory (DFT) using the pseudopotential augmented plane-wave basis as implemented in VASP[26–28] with the Perdew-Burke-Ernzerhof exchange-correlation functional[29], a plane-wave energy cutoff of 520 eV, and a 9×9×9 Monkhorst-Pack k-grid. The resulting crystal structure corresponds to a lattice constant of 8.46 Å and occupied Wyckoff positions: 8a (1/8, 1/8, 1/8) for Li, 16d (1/2, 1/2, 1/2) for Ti, and 32e (0.26205, 0.26205, 0.2l205) for O.

DFT-based electronic structure calculations were performed using the augmented plane-wave, pseudopotential code QUANTUM ESPRESSO (v7.3)[30,31] with the Perdew-Burke-Ernzerhof version[29] of the generalized gradient approximation as the exchange-correlation functional. The plane-wave basis is set with a wavefunction cutoff of 60 Ry (the charge density cutoff was set to 720 Ry). Brillouin zone integration was carried out on a $12\times12\times12$ k-grid with a Methfessel-Paxton smearing of 0.02 Ry.

To better treat the local electronic correlations, DFT+dymanical mean-dield theory (DMFT) calculations were performed. We downfold onto the Ti t_{2g}-like Kohn-Sham bands using Wannier functions as implemented in Wannier90[32], which defines the DMFT impurity problem. Interactions of the Hubbard-Kanamori form govern the impurity problem. We

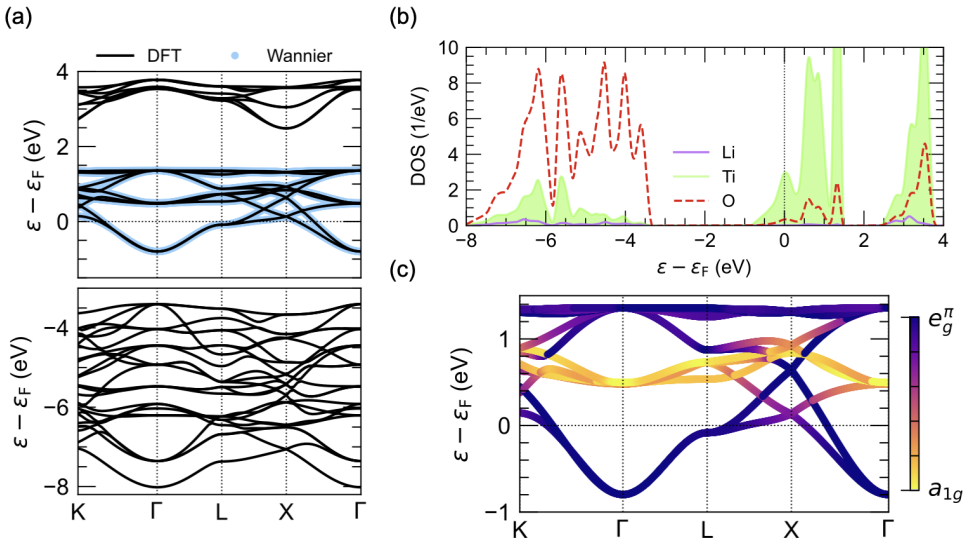

FIG. S12. DFT data for $LiTi_2O_4$. (a) Band structure along high-symmetry lines (black lines) compared with the band structure representation of the Wannier basis (blue). (b) Atom-resolved density of states (DOS). (c) Orbital-projected band structure representing the a_{1g} and e_g^π-like bands.

sweep over a range of U values keeping J fixed to 0.68 eV (and $U' = U - 2J$). The inverse electronic temperature was set to $\beta = 80$ eV^{-1} (T = 145 K). Real-frequency data for the self-energy is obtained using Padé analytic continuation. The DFT+DMFT calculation is one-shot meaning that there is no feedback from the DMFT calculation to update the DFT charge density. The "double-counting" term is absorbed into the chemical potential, since we work only the low-energy space spanned by the Ti-t_{2g}-like Wannier orbitals.
The DMFT calculation incorporates all local quantum fluctuations for the Ti-t_{2g} impurity that we consider here. This means that we have access to all of the atomic multiplets and the probability of the impurity being found in a given multiplet. Figure S13 shows a histogram of the atomic multiplets for the Ti impurity, where N denotes the total number of electrons in the 3 t_{2g}-like orbitals. The histogram reflects the mixed-valence nature of the spinel oxide with about equal probability for the $N = 0$ (d^0) and $N = 1$ (d^1) atomic configurations.

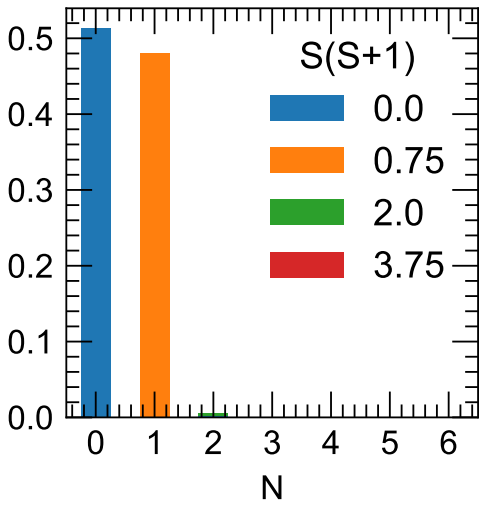

FIG. S13. Atomic histogram for the t_{2g} considered for $LiTi_2O_4$ obtained directly from measuring the density matrix within the continuous-time quantum Monte Carlo impurity solver.

Lattice dynamics are computed within density-functional perturbation theory (DFPT)[33] as implemented in the QUANTUM ESPRESSO package[30,31] using a $3 \times 3 \times 3$ q-grid. We use the EPW code[34,35] using the Wannier intepolation method[36] to compute the electron-phonon (e-ph) interactions, e-ph self-energy, and (e-ph) spectral functions.

Electronic structure. The electronic structure of $LiTi_2O_4$ obtained from DFT calculations, displayed in Fig. S12(a,b), consists of a narrow manifold of the Ti-t_{2g} bands near the Fermi level with an overall bandwidth ~ 2.5 eV, which are well separated from a complex of O($2p$) bands near -4 eV. The unoccupied Ti-e_g are centered around $+3$ eV. The orbital content of the Ti-t_{2g}-like bands is shown in Fig. S12(c), which reveals a narrow a_{1g} band around $+1$ eV flanked above and below by broad bands of e_g^π character (the trigonal distortion of the TiO_6 octahedra splits the Ti($3d$) orbitals into an a_{1g}, two degenerate e_g^π orbitals, and two

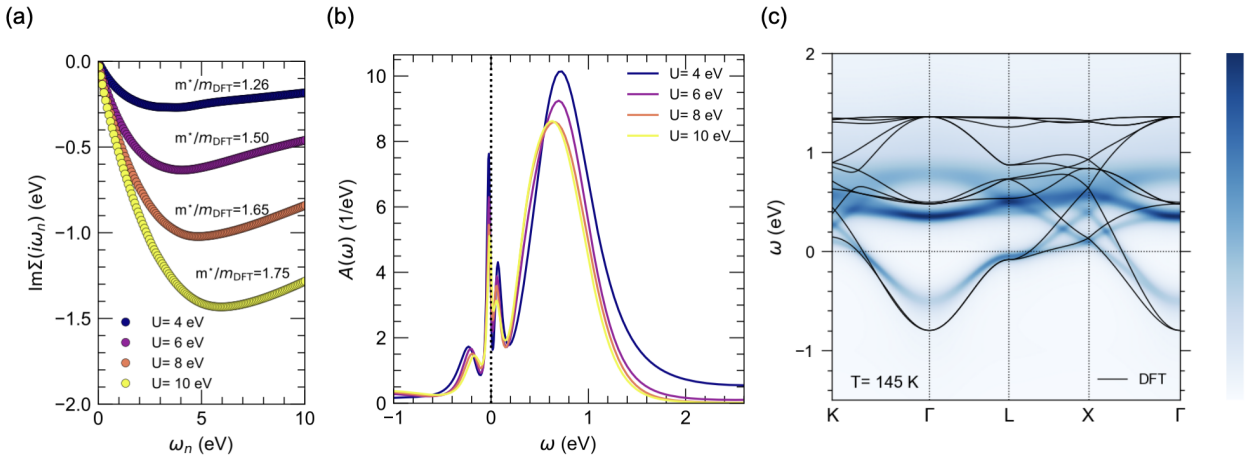

FIG. S14. Summary of additional DMFT data for $LiTi_2O_4$ performed at $\beta = 80$ eV^{-1} ($T = 145$ K). (a) Imaginary part of the Matsubara self-energy averaged over all orbitals for different choices of U. (b) Total spectral function for different choices of U. (c) Momenutm-resolved spectral function along high-symmetry lines for $U = 8$ eV. Solid lines denote the DFT band structure.

degenerate e_g orbitals with the a_{1g} and e_g^π comprising the formal t_{2g} cubic basis.)

Figure S14 shows the Hubbard U dependence of the DMFT solutions to the quantum impurity problem. The imaginary part of the Matsubara self-energy is shown in Fig. S14(a) with the mass enhancement estimated from the inverse quasiparticle renormalization factor $m^\star/m_{\rm DFT} = 1/Z = (1 - \partial_{\omega_n} {\rm Im}\Sigma(i\omega_n)|_{\omega_n \to 0})^{-1}$ by fitting a fourth-order polynomial to the lowest 6 Matsubara points. The total spectral function $A(\omega)$ as a function of Hubbard U displayed in Fig. S14(b) shows a narrow quasiparticle peak at the chemical potential with small shoulders above and below comprising the upper and lower Hubbard bands. Figure S14(c) shows the momentum-resolved spectral function, $A(\mathbf{k}, \omega)$ at $U = 8$ eV compared with the DFT bands (solid, black lines). The DMFT dataset for $U = 8$ eV seems to reproduce the observed mass renormalization from ARPES, therefore, we present the data for this choice of U in the main text. However, we acknowledge that this choice of U is ad hoc and should not be taken as a spectroscopic U value, but rather an internal parameter that can be tuned in the DFT+DMFT calculations.

Figure S15(a) displays the temperature dependence of the "kink" due to electron-phonon interactions in $LiTi_2O_4$, as well as the corresponding self-energy (Fig. S15(b)). We compare the self-energies from electron-phonon interactions (el-ph) and DMFT (el-el) in Fig. S14, where we make a few observations: the slope around $\omega = 0$ for ReΣ is much larger for $\Sigma^{\text{el-el}}$ indicating stronger electronic correlations, there is a sharp change in derivative in Re$\Sigma^{\text{el-ph}}$ which is responsible for the "kink" in the dispersion, and the scattering rate ($\propto$ Im$\Sigma(\omega = 0)$) is much larger for $\Sigma^{\text{el-el}}$ than $\Sigma^{\text{el-ph}}$, which is another signal of strong electron-electron interactions in this material.

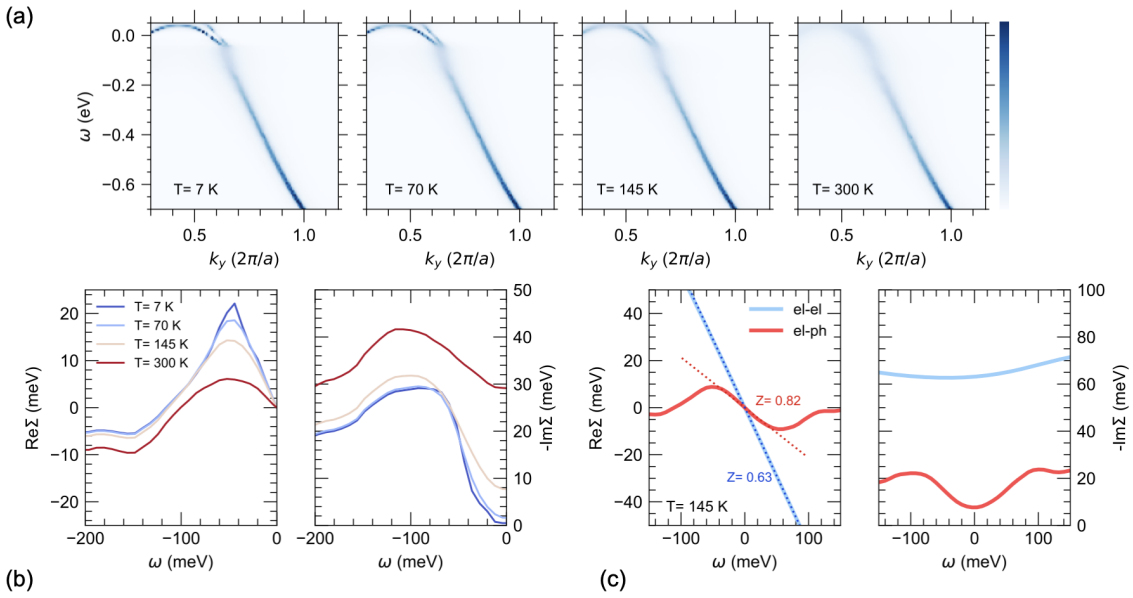

FIG. S15. Summary of electron-phonon data for $LiTi_2O_4$. (a) Temperature dependence of the "kink" feature in the spectral function. (b) Real (left) and imaginary (right) parts of the electron-phonon self-energy for different temperatures. (c) Comparison of the electron-phonon and electron-electron (DMFT) self-energies at $T = 145$ K.

S6. SUPPLEMENTARY NOTE 6: RESONANT INELASTIC X-RAY SCATTERING

Resonant inelastic x-ray scattering was performed at I-21 at the Diamond Light Source and at SIX at NSLS-II. Data from both beamlines is shown in Fig. S16 and is in excellent agreement with each other. Data at Diamond was collected in the $2\theta = 90^0$ and $\theta = 20^0$, while the spectra at SIX is collected in the $2\theta = 150^0$ and $\theta = 20^o$ confuguration.

A. Fitting low-energy RIXS spectra

We can use the Ament Model to fit local, non-dispersive Einstein phonons. We start with the Frohlich Hamiltonian:

$$H = M \sum_R d_R^\dagger d_R (b_R^\dagger + b_R) + \hbar\omega_o \sum_R b_R^\dagger b_R \tag{S9}$$

where M represents the electron-phonon coupling energy for a phonon mode of strength $\hbar\omega_o$, and $d_R^\dagger$ ($b_R^\dagger$) and d_R (b_R) are the creation and annihilation operators for electrons (phonons) respectively. Diagonalizing this Hamiltonian (details of which can be found in Ref.[37]) leads us to the RIXS amplitude for exciting n' phonons when starting from the ground state. The

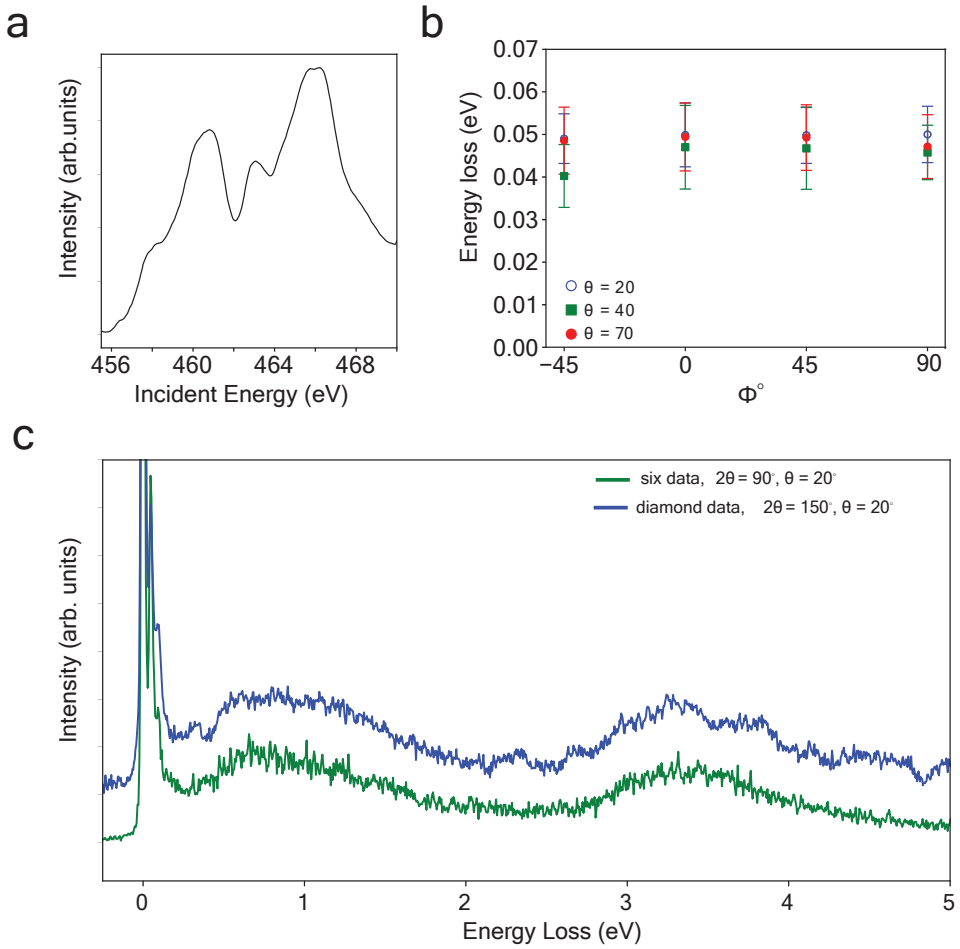

FIG. S16. **a**, XAS at the Ti-$L_{3,2}$ edge. **b**, Dispersion of phonon modes as a function of ϕ. Different symbols correspond to different θ values. **c**, Full RIXS spectra at the Ti-L_3 edge at I-21 in Diamond Light Source and at SIX in NSLS-II.

amplitude for the n'th phonon can be written as follows:

$$A = \sum_{n=0}^{\infty} \frac{B_{max(n',n),min(n',n)}(g) B_{n0}(g)}{\Omega_{det} + i\Gamma + (g-n)\omega_o} \tag{S10}$$

where the Franck-Cordon factors in the numerator are functions of the form

$$B_{mn}(g) = (-1)^m \sqrt{e^{-g} m! n!} \sum_{l=0}^{n} \frac{(-g)^l \sqrt{g}^{m-n}}{(n-l)!\, l!\, (m-n+l)!}$$

Here $g = \frac{M^2}{(\hbar\omega_o)^2}$ is the dimensionless electron-phonon coupling strength, Ω_{det} is the energy detuning, and Γ is the inverse core-hole lifetime. To fit our RIXS spectra (Fig. 3e and f), we can set $\Omega_{det} = 0$ due to the excellent incident energy calibration from the beamlines. We also fix Γ to be 375 meV for titanium and 235 meV for oxygen as determined from previous XAS experiments[38,39].

Our RIXS spectra (Fig. 3e and f) can then be well fit by a Voigt function for the elastic feature, a Lorentzian with amplitude described above for the phonon satellites multiplied by a scaling factor, a small background, as well as a broad anti-symmetrized Lorentzian to capture the incoherent phonons that cannot be distinguished within the energy resolution of the beamline. Our model parameter g, and the center of the Lorentzian(s) parametrizing the energy of the phonon satellites is set to vary. Our best fit for the titanium and oxygen spectra then give us $g_{Ti} = 9.0 \pm 3.0$ with $\omega_o = 47 \pm 2$ meV and $g_O = 6.89 \pm 3.17$ corresponding to $\omega_o = 71 \pm 1$ meV.

B. Phonon modes probed via RIXS

To corroborate the quasi-elastic phononic nature of the excitations in Fig. 3e, we present linear vertical (LV) and linear horizontal (LH) polarization data for the Ti-L edge. In this geometric configuration ($2\theta = 90°$, $\theta = 45°$), charge excitations are suppressed in the LH polarization due to Thompson scattering. As shown below, we observe a near complete suppression of the phonon modes in the LH data compared to the LV data, further corroborating that these excitations are phononic in nature.

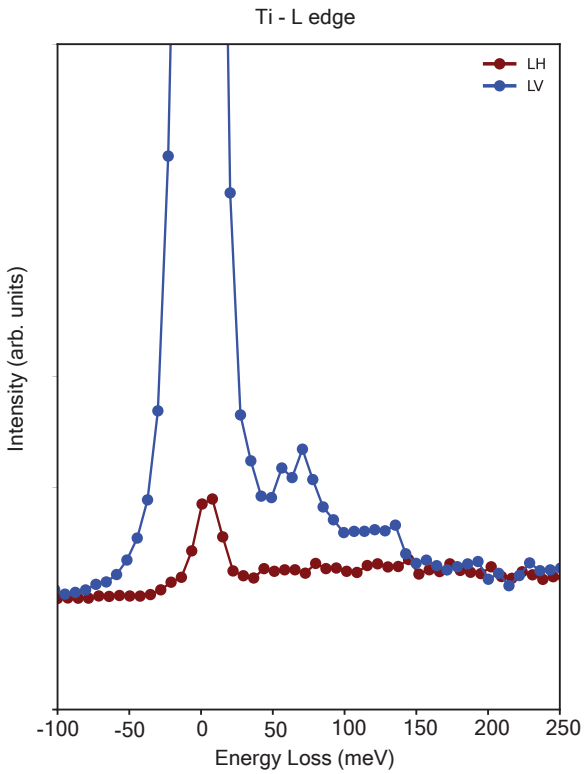

FIG. S17. Ti-L edge RIXS spectra in linear horizontal (LH) and linear vertical (LV) polarization in $2\theta = 90°$, $\theta = 45°$ configuration at 22 K. LH shows a complete suppression as is expected for phonon excitations.

We now turn our attention to the presence of different phonon modes at the O-K edge and the Ti-L edge. In the text below, we reason why the E_g mode dominates at the Ti-L edge and the A_{1g} mode at the O-K edge. Since RIXS at the Ti-L_3 edge is sensitive to changes in the local environment and our RIXS at the O-K edge demonstrates strong O-Ti hybridization, the observation of the oxygen E_g mode at the Ti-L_3 can be understood from a symmetry point of view. While an E_g distortion reduces the D_{3d} point group of the titanium atom, the A_{1g} is a symmetry-conserving breathing mode. This can be seen in Fig. S18. We note that the observation of an oxygen phonon mode at the Ti-L edge is a strong indication of polaronic physics, as it indicates a very strong coupling between the oxygen vibrations and the local electronic structure of the titanium atoms.

Regarding the lack of coherence of the E_g mode at the O-K edge and the dominant intensity from the A_{1g} mode, our data suggests that the E_g coherence at the O-K edge is impeded by the high density of oxygen phonon modes at $\approx$ 46meV, as shown in Fig. 3h of the main text. Instead, these phonons manifest as spectral intensity captured by a broad Gaussian centered at the E_g mode at E$\approx$ 46 meV. Thus, the O-K edge shows a dominant, coherent A_{1g}

mode and an incoherent background which includes the E_g mode among other unresolvable phonon modes.

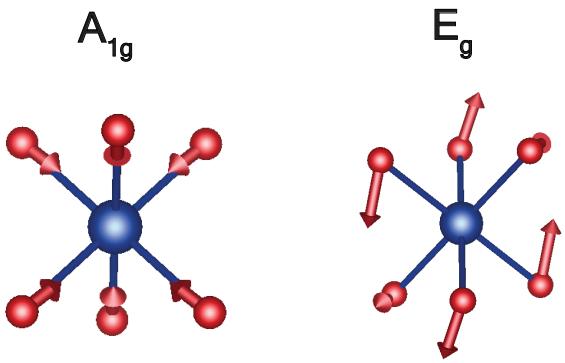

FIG. S18. Comparing the effect of E_g phonon mode with A_{1g} phonon mode on an isolated titanium octahedra.

C. Multiplet ligand calculations

In this section, we show local multiplet ligand calculations for a Ti d^1 ions with different crystal field enviroments. The left pannel of Fig. S19 shows the calculated RIXS intensity

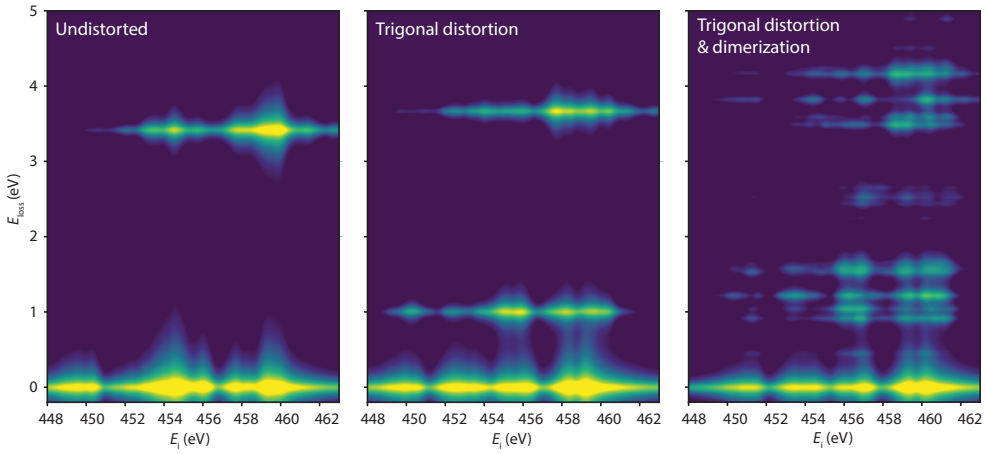

FIG. S19. Calculated Ti d^1 $L_{3,2}$ RIXS intensity from exact diagonalization calculations of the crystal field multiplet excitations of (left) a single Ti site in a cubic crystal field, (center) a trigonally distorted Ti single site and (right) a trigonally distorted Ti-Ti dimer.

using the EDRIXS software package[40] with a cubic crystal field $D_q = 0.34$ eV. In a second model, following the calculations in Ref.[41], we including the effects of a non-cubic trigonal crystal field in the total d-shell. The CF part of the Hamiltonian in the spherical Harmonic basis[42] including cubic and trigonal fields is given by:

$$H_{CF}^{D_{3d}} = \begin{pmatrix} a_{0,0} & 0 & 0 & a_{0,3} & 0 \\ 0 & a_{1,1} & 0 & 0 & a_{1,4} \\ 0 & 0 & a_{2,2} & 0 & 0 \\ a_{3,0} & 0 & 0 & a_{3,3} & 0 \\ 0 & a_{4,1} & 0 & 0 & a_{4,4} \end{pmatrix}, \tag{S11}$$

with:

$$a_{0,0} = a_{4,4} = -3C_p\mathscr{P}_1(\cos\alpha) + (3/14)D_q\mathscr{P}_2(\cos\alpha), \tag{S12a}$$
$$a_{0,3} = a_{3,0} = -a_{1,4} = -a_{4,1} = 15D_q \sin\alpha^3 \cos\alpha, \tag{S12b}$$
$$a_{1,1} = a_{3,3} = (3/2)C_p\mathscr{P}_1(\cos\alpha) - (6/7)D_q\mathscr{P}_2(\cos\alpha), \tag{S12c}$$
$$a_{2,2} = 3C_p\mathscr{P}_1(\cos\alpha) + (9/7)D_q\mathscr{P}_2(\cos\alpha), \tag{S12d}$$

with $\mathscr{P}_1(\alpha)$ and $\mathscr{P}_2(\alpha)$ the $n = 1$ and $n = 2$ Legendre polynomial with $x = \cos\alpha$. When written in the d- orbital basis D_q encodes the splitting between e_g and t_{2g} levels. α parameterizes the size of the trigonal distortion, with $\alpha_0 = 54.74°$ for a perfect octahedral environment, and C_p is the value of the non-cubic crystal fields due to trigonal distortion. While C_p is hard to model, realistic values of C_P follow $|C_p| < 0.17D_q$[43]. Based on the structural parameters $\alpha = 54.5°$ in $LiTi_2O_4$. The effects of the trigonal distortion for unphysical values of $\alpha = 45.5°$ and $C_p = -0.5D_q$ are shown in the middle panel of Fig. S19.

Lastly, a Ti-Ti dimer is considered by introducing a term in the Hamiltonian given by:

$$H^{12} = \begin{pmatrix} t_{e_g} & 0 & 0 & t_{e_g} & 0 \\ 0 & 0 & t_{e'_g} & t_{e'_g} & 0 \\ 0 & 0 & t_{e'_g} & t_{e'_g} & 0 \\ t_{e_g} & 0 & 0 & t_{e_g} & 0 \\ 0 & 0 & 0 & 0 & t_{a_{1g}} \end{pmatrix} + c.c. \tag{S13}$$

in the $(d_{z^2}, d_{zx}, d_{zy}, d_{x2-y2}, d_{xy})$ basis that parametrizes the off-diagonal hopping between two neighboring Ti sites with $t_{e_g} = t_{e'_g} = 0.72$ eV and $t_{a_{1g}} = 0.9$ eV. The corresponding RIXS intensity, which shows qualitative agreement with our RIXS data, are shown in the right panel of Fig. S19. For all the calculations $U_{dd} = 3.5$ eV, $U_{dp} = 4$ eV. The calculated slatter parameters $F^2_{dd}, F^4_{dd}, F^2_{dp}, G^1_{dp}, G^3_{dp}$ are rescaled by $f = 0.8$ with respect to the single ion values.

S7. SUPPLEMENTARY NOTE 7: MUON SPIN RELAXATION

To understand the interactions between magnetism and superconducting order in high-quality $LiTi_2O_4$ films, we proposed low-energy muon spin-relaxation (LE-μSR) measurements using the LEM instrument at the Swiss muon source. Unlike bulk muon spin relaxation techniques that implant 4 MeV muons deep into bulk materials, LE-μSR implants spin-polarized μ^+s with relatively low kinetic energies (1 keV – 30 keV) to achieve mean implantation depths ranging from approximately 10 nm – 300 nm. In our case, we measured a single 28 nm thick $LiTi_2O_4$ film grown on a $MgAl_2O_4$ substrate and simulated the expected μ^+s stopping profiles of various energies, shown in Figure S20(a). Based on these simulations, we selected an implantation energy of 2.5 keV, placing the peak of the μ^+s stopping profile in the bulk of the film at approximately 18 nm.

Measurements were performed in an applied magnetic field of approximately 10 mT transverse to the μ^+s spin polarization direction (field cooling). Upon stopping in the film, the μ^+s spin precesses about local magnetic fields before decaying into a positron, electron neutrino, and muon antineutrino with a characteristic lifetime of approximately 2.2×10^{-6} s. The positron is emitted preferentially along the direction of the μ^+s, so that the μ^+s spin-polarization direction (and hence the local field environment) may be probed as a function of time by measuring the time-dependent direction asymmetry of the positron emission. Specifically, in a temperature-dependent measurement series we may fit the directional asymmetry of positrons detector at time t and temperature T using the function:

$$A(t,T) = A_{NM}(T)e^{(-\lambda(T)t)}cos(\omega_L t) \tag{S14}$$

Where A is the asymmetry, λ is the muon depolarization rate, ω_L is the Larmor precession frequency, and A_{NM} is the asymmetry at high-temperature in a nonmagnetic, non-superconducting state. Here, the selection of a temperature for A_{NM} is critical, as Li ions are known to become mobile above 200 K to an extend that μSR measurements are affected by the motion[44,45]. We therefore selected the maximum temperature of 190 K as our baseline. Example time-dependent data and theoretical fits are shown in Figure S20(b) for the maximum (190 K) and minimum (5 K) measured temperatures, where significant differences are observed after entering the superconducting state. The temperature-dependent extracted parameters of asymmetry, magnetic field (determined from ω_L), and depolarization rate are shown in Figure S20(c)-(e).

For the detection of magnetic order, the asymmetry value is particularly useful, and any μ^+s stopping in a region of the film hosting static magnetic order will experience a broad magnetic field distributions which depolarize the μ^+ on a timescale much faster than the measurement time. These μ^+s do not contribute to the measure asymmetry and effectively go "missing" so that A in a magnetically ordered state is expected to be lower than in a nonmagnetic condition. We may then determine the magnetically ordered volume fraction in

the material by normalizing to the baseline asymmetry measured in a nonmagnetic state and account for μ^+s which stop in the nonmagnetic substrate. The magnetically order volume fraction FM is therefore

$$F_M(T) = (1 - \frac{A(T)}{A(190K)})\frac{1}{F_{LTO}} \tag{S15}$$

Where F_{LTO} is the fraction of μ^+s stopping in the $LiTi_2O_4$. At 2.5 keV, F_{LTO} is calculated to be 97.8%. Fitting the temperature-dependent asymmetry to an order parameter function for all data in the range 10 K $\leq$ T $\leq$ 190 K, as shown in the red dotted line of Figure S20(c) yields a low-temperature magnetically ordered volume faction of 8.2% $\pm$ 0.6%, with a transition temperature of 84 K $\pm$ 12 K. The presence of a small magnetically ordered volume within the film is clearly statistically significant, and the resulting transition temperature is within two standard deviations of a previously reported magnetic transition in $LiTi_2O_4$[11]. K. Jin *et al.* reported magnetic susceptibility and magneto-transport measurements which point towards two distinct magnetic transitions in $LiTi_2O_4$[11]. Specifically, at 100 K $\pm$ 10 K they report increased susceptibility and twofold symmetry in the anisotropic magnetoresistance. At 50 K $\pm$ 10 K they report a sign change in the magnetoresistance consistent with our observations.

Because modeling the temperature-dependent F_M as a single transition yields an unexpectedly broad transition, we performed an alternative fit to the data which presumed two distinct magnetic transition, as in Jin *et al.*[11]. This model fits the temperature-dependent asymmetry data slightly better than a single transition, with χ^2 decreasing from 2.26 to 2.16 and sharper transitions. While we do not regard this improvement to the fit as definitive, the fitted transition temperatures are an excellent match for those previously reported by Jin *et al.* at 94 K $\pm$ 9 K and 53 K $\pm$ 7 K. Thus, we suspect that the experiments of Jin et al. were detecting the influence of a minority magnetic phase which can be present in $LiTi_2O_4$ films, affecting approximately 8% of the film. This interpretation is strengthened by the observation that the magnetic field experienced by the muons increases abruptly at approximately 100 K, as shown in Figure S20(d), rather than at 84 K as implied by the "single transition" fit. We note again, however, that the 95% confidence interval for the transition temperature in the "single transition" model includes 100 K, so the two models are challenging to distinguish. Regardless, the observed sharp change in internal field is an excellent match for the higher-temperature transition in Jin et al. On the other hand, there are no sharp transitions observed in λ above the superconducting critical temperature. Rather, λ increases slowly and roughly linearly from 190 K to 10 K, with an approximate slope of -0.52$\times 10^{-6}$ μs/K $\pm$ 0.18$\times 10^{-6}$ μs/K. Note that the fits to asymmetry and λ both fail to describe the data at 5 K due to the emergence of a vortex lattice state, which is not well-described by our fitting functions.

Below the superconducting critical temperature, we observed sudden increases in the internal magnetic field to nearly 10.3 mT and a nearly fivefold increase in the damping rate.

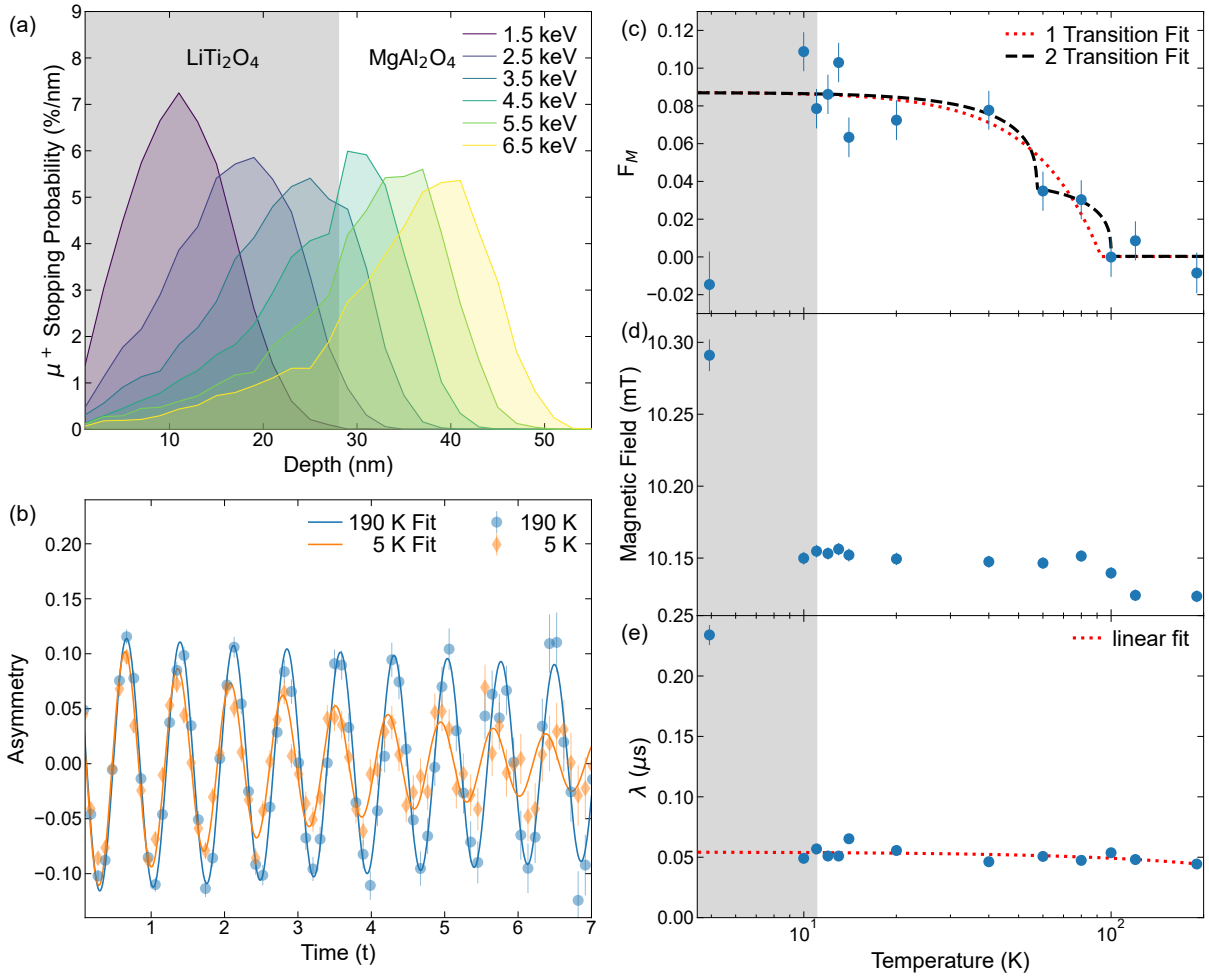

FIG. S20. (a) Muon implantation simulations showing the μ^+ stopped probability as a function of depth for a range of μ^+ kinetic energies. (b) Asymmetry vs. time measurements for the $LiTi_2O_4$ film at 190 K and at 5 K alongside theoretical fits to the data. (c) Temperature-dependent magnetically ordered volume fraction of the $LiTi_2O_4$ film, as extracted from fits to the LE-μSR data. (d) Most probable internal magnetic field experienced by μ^+s as a function of temperature. (e) Muon depolarization rate vs. temperature.

The increased damping rate originates from the magnetic flux vortex lattice as previously reported[46]. The increase in the internal magnetic field is unexpected, as the observed value should be dominated by the most probable field of the vortex lattice, which is smaller than the applied field.

S8. SUPPLEMENTARY NOTE 8: SCANNING TRANSMISSION ELECTRON MICROSCOPY

Simulated ADF-STEM images (Fig. S22b and c and Fig. S23b) were generated with quantum mechanically accurate multislice algorithms using abTEM[47] package.

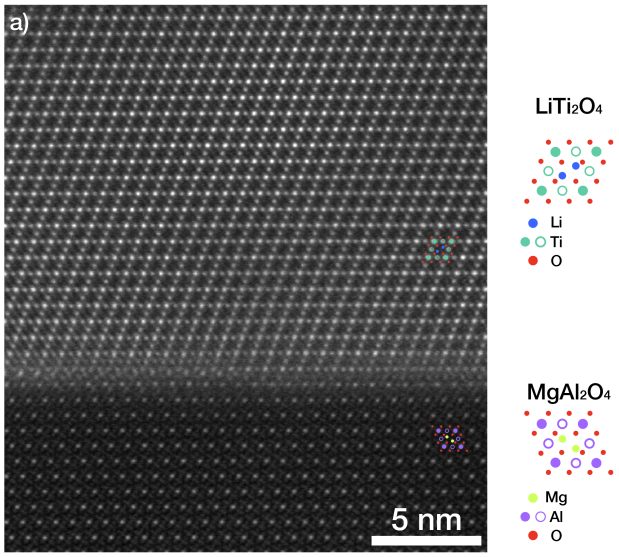

FIG. S21. Atomic resolution ADF-STEM image shows clean $LiTi_2O_4/MgAl_2O_4$ interface.

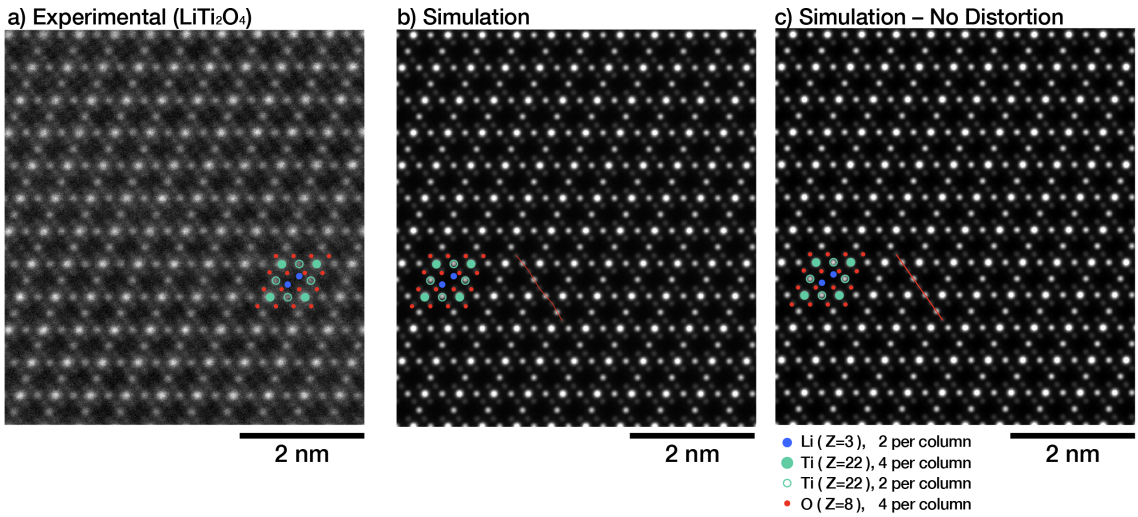

FIG. S22. a) Experimental ADF-STEM image of $LiTi_2O_4$ thin film and simulated image b) with and c) without trigonal distortions. b, c) With trigional distortion, the oxygen-titanium plane (marked red) forms a subtle zig-zag pattern. In experimental data (a), zig-zag pattern is subtle and not detectable.

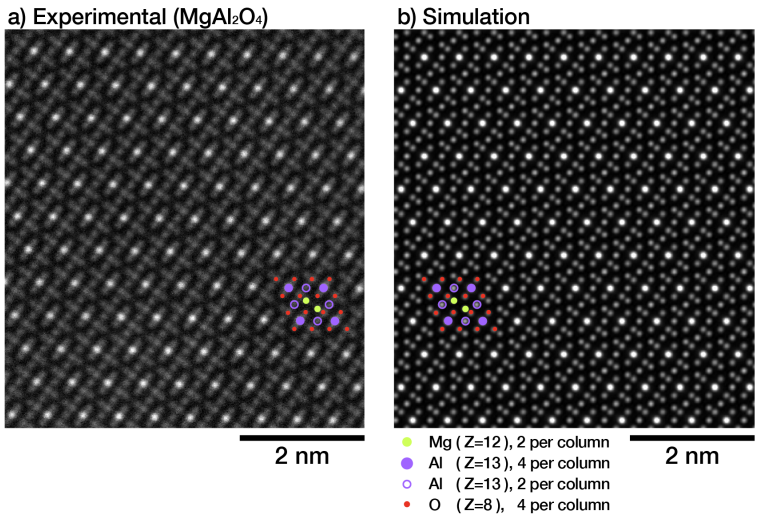

FIG. S23. a) Experimental and b) simulated ADF-STEM image of $MgAl_2O_4$ substrate.

We also attempt to characterize the presence of Li/Ti antisite defects via STEM imaging. Our zoomed out HAADF-STEM image in Fig. 1d shows uniform crystallinity over a large area of the film. Additional STEM imaging in Fig. S24 below also shows that within a large field of view, the film is relatively defect free. The quantitative ratio of the presence of defects and the Li/Ti ratio cannot be established due to the beam sensitivity of the light lithium atoms as shown in Fig. S24b and S24c. Nevertheless, our qualitative conclusion of a relatively defect free, stoichiometric $LiTi_2O_4$ thin film is backed up by several observations and comparisons to literature. Firstly, lithium deficiency where x = -0.1 and -0.2 in $Li_{1+x}Ti_{2-x}O_4$ are outside of the spinel homogeneity range and would be evident in an X-ray diffraction as a secondary (Ti,Li)O_x phase[48]. Considering our smooth RHEED pattern, as well as phase pure X-ray diffraction patterns (Fig. S1a), we can rule out Li-deficiency in our thin films. For lithium excess, reference[48] and reference[49] note that $Li_{1+x}Ti_{2-x}O_4$ shows higher room temperature resistivity as well as semiconducting behavior as x is increased from $0 \leq x \leq \frac{1}{3}$. Not only is the room temperature resistivity of our films consistent with the room temperature resistivity of other high quality thin films[23,50], our films are also metallic all the way down to a sharp superconducting transition which is consistent with having high quality stoichiometric thin films with $x = 0$ in $Li_{1+x}Ti_{2-x}O_4$[48,49]. Finally, our lattice constants as established by reciprocal space maps and x-ray diffraction patterns (a = 8.40 Å) fall within the stoichiometric ratio expected for bulk $LiTi_2O_4$: deviations from stoichiometry would result in a smaller lattice constant as shown in Fig. 4 in reference[48,49]. Thus, we can conclude that within the possible ways of establishing stoichiometric ratio of Li/Ti in $LiTi_2O_4$, our films fall well within the stoichiometric ratio expected for $LiTi_2O_4$.

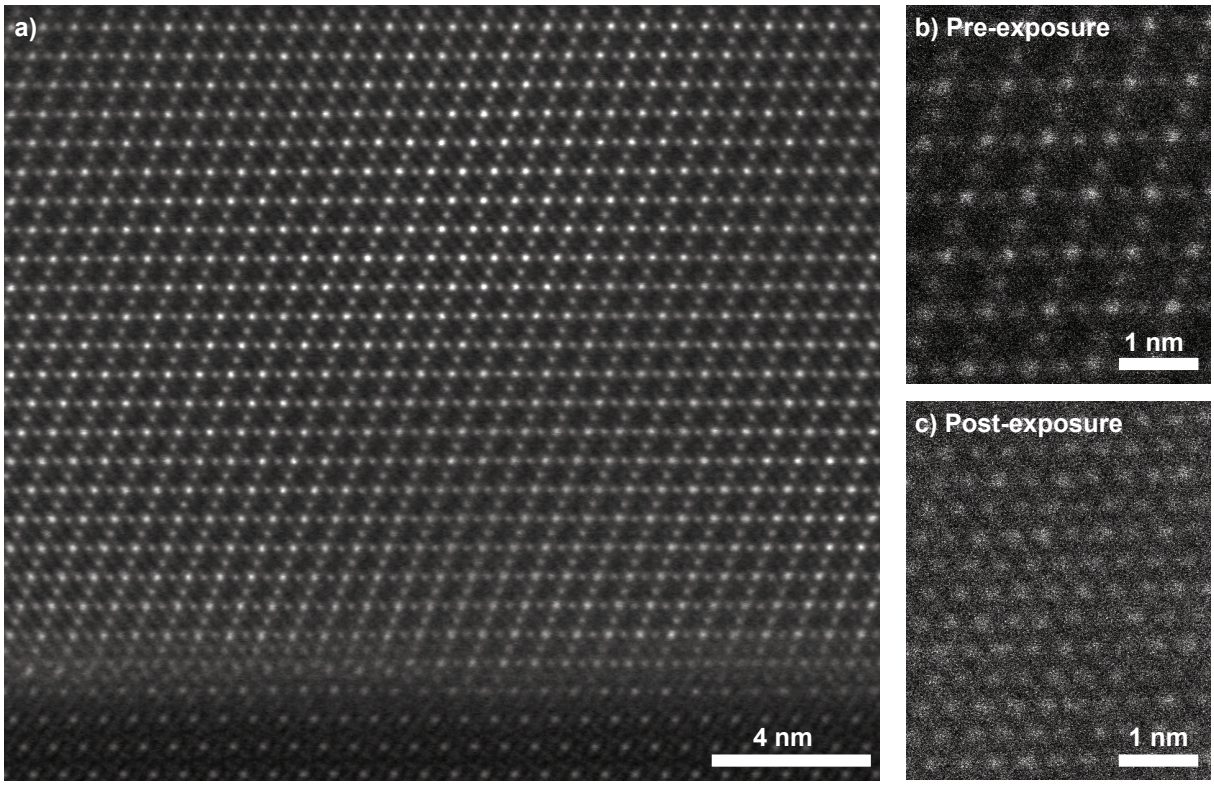

FIG. S24. Radiation sensitivity of $LiTi_2O_4$ thin film. a) Large-area TEM image of the high quality as-grown film, showing a uniform, defect-free microstructure. b, c) High-resolution TEM images taken from the same region before (b) and after (c) electron beam exposure. The crystal structure undergoes significant rearrangement under irradiation, likely driven by knock-on damage to the light lithium atoms. Images were acquired at 200 keV with a probe current of 40 pA, a dwell time of 200 ns per pixel, and a scan resolution of 1024 x 1024 pixels. (b) and (c) correspond to the 1st and 40th frames, respectively, during continuous scanning.

S9. SUPPLEMENTARY NOTE 9: X-RAY ABSORPTION SPECTROSCOPY:

Figure S25i) compares the Ti-L edge spectra to a reference Ti^{4+} spectra ($SrTiO_3$)[51] and a reference Ti^{3+} spectra ($YTiO_3$)[51], as well as another $LiTi_2O_4$ thin film[5]. The Ti-L edge spectra have been aligned to two dotted blue lines corresponding to the pre-edge feature labeled L_{pre} and the first t_{2g} peak (labeled t_{2g}). With this alignment, we can see that our uncapped $LiTi_2O_4$ thin film resembles the PLD grown $LiTi_2O_4$ thin film[5] as well as other $LiTi_2O_4$ powder spectra[52] (not shown here). The analysis in reference[5], assigns the qualitative features such as the intensity of the pre-peak as well as the merging of the t_{2g} and e_g peaks as a signature of the mixing of Ti^{3+} and Ti^{4+} oxidation states. The reference $LiTi_2O_4$ thin film spectra is extremely similar to our uncapped $LiTi_2O_4$ thin film

spectra, showing that our uncapped results are consistent with literature where $LiTi_2O_4$ is also uncapped. However, $LiTi_2O_4$ is known to be air and moisture sensitive and prone to "aging", as discussed in references[53,54]. The result of such a degradation process would lead to surface oxidation with excess Ti^{4+} on the surface of any $LiTi_2O_4$ crystal or powder. Since the spectra in Fig. S25 are measured in the surface sensitive total electron yield (TEY) configuration, all the uncapped $LiTi_2O_4$ thin films show a higher concentration of Ti_{4+} than would be native to $LiTi_2O_4$. Thus, our $LiTi_2O_4$ capped thin film represents a more pristine surface which is more representative of the native oxidation state in $LiTi_2O_4$. We can see that the capped $LiTi_2O_4$ thin film has a higher Ti^{3+} content, with a pronounced pre-edge feature as well as further merging of the t_{2g} and e_g states highlighting its Ti^{3+} content.

Since the comparison data in Fig. S25 were collected at different beamlines and times with varying incident-energy calibrations, any observed energy shifts cannot be used to quantitatively determine the titanium oxidation state in our films. In addition, because the intensity axis was already offset in the spectra taken from Ref.[5,51,52], the relative intensities of specific features cannot be meaningfully compared across spectra. Nevertheless, we can put bounds on what the titanium oxidation can be by looking at the O-K edge. Figure S25ii) shows the O-K edge XAS spectra of $LiTi_2O_4$ powders and thin films for comparison with our capped and uncapped data. We can see that our capped data shows the first two peaks which are indicative of oxygen-titanium hybridization features, also observed in the uncapped data and the reference literature[52], after which the SiO spectra dominates the O-K edge. However, the first two pre-peaks can be used to bound the titanium oxidation state in $LiTi_2O_4$. Looking at the $LiTi_2O_4$ powder[52] for comparison, we can see that as titanium moves more towards Ti^{3+} with excess lithium, the two pre-edge hybridization features in the O-K edge seem to merge, which is inconsistent with our $LiTi_2O_4$ thin film data. The stoichiometry of our samples is further corroborated with our T_c of $\approx$ 12 K and lattice constant of a = 8.40 $\AA$, which is within the stoichiometric bounds that give this T_c and lattice constant as shown in reference[49] - any higher than a 5 percent excess of lithium would decrease the superconducting T_c and the lattice constant. Furthermore, lithium deficiency is outside of the spinel homogeneity range and results in (Li, Ti)O_x secondary phases which are absent from our x-ray diffraction (XRD) data which shows phase pure $LiTi_2O_4$ (Fig. S1). Thus, while small uncertainties cannot be absolutely ruled out, our XRD data, lattice constant, XAS data and superconducting transition temperature are all consistent with having stoichiometric $LiTi_2O_4$ thin films with a mixed-valence $Ti^{3.5+}$.

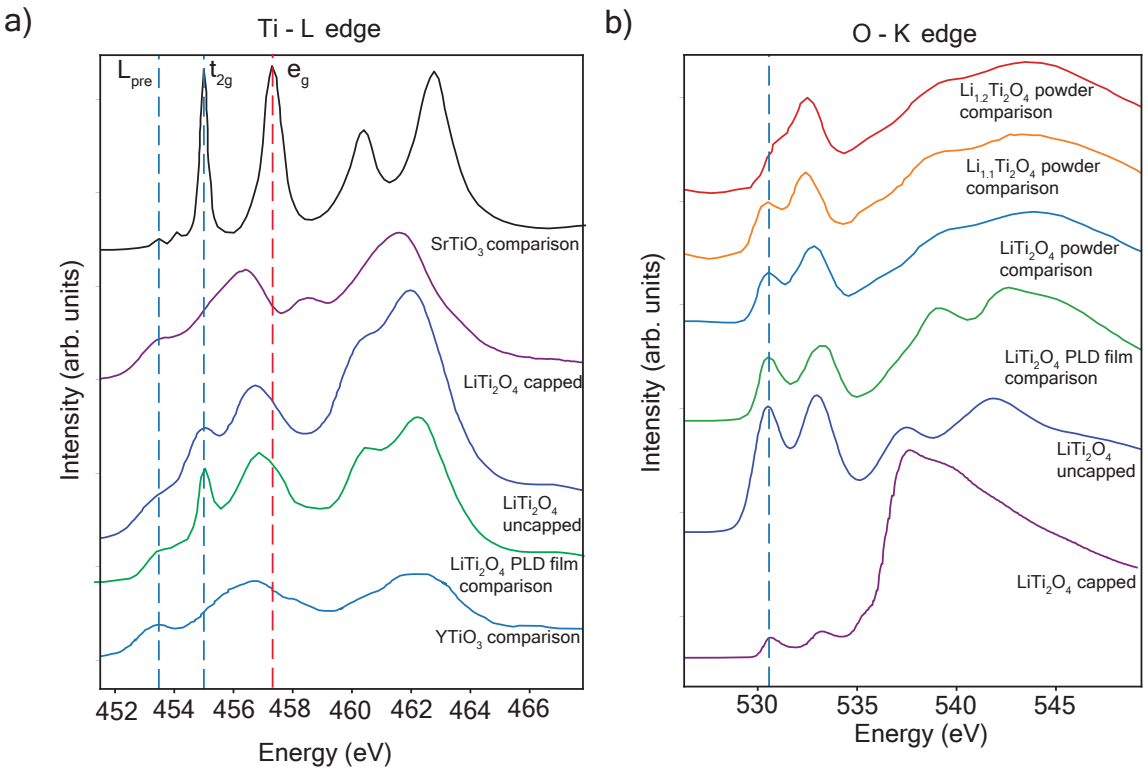

FIG. S25. X-ray absorption spectroscopy of reference spectra for comparison to $LiTi_2O_4$. Our work is labelled as "$LiTi_2O_4$ capped" denoting a $LiTi_2O_4/MgAl_2O_4$ (111) thin film with a $\approx$ 5 nm SiO cap and and "$LiTi_2O_4$ uncapped" which is without the SiO cap. **a**) Ti-L edge spectra. $SrTiO_3$ and $YTiO_3$ have been adapted from[51] whereas the $LiTi_2O_4$ thin film comparison is from[5]. **b**) O-K edge spectra. Stoichiometric and excess lithium $LiTi_2O_4$ powders have been adapted from[52], whereas the thin film comparison is from[5].

[1] Chris D Theis and Darrell G Schlom. Cheap and stable titanium source for use in oxide molecular beam epitaxy systems. *Journal of Vacuum Science and Technology-Section A-Vacuum Surfaces and Films*, 14(4):2677–2679, 1996.

[2] DJ Harra and TW Snouse. A radiant heated titanium sublimator. *Journal of Vacuum Science and Technology*, 9(1):552–555, 1972.

[3] Wolfgang Braun and Jochen Mannhart. Film deposition by thermal laser evaporation. *Aip Advances*, 9(8), 2019.

[4] Yuita Fujisawa, Anjana Krishnadas, Chia-Hsiu Hsu, Barnaby RM Smith, Markel Pardo-Almanza, Yukiko Obata, Dyon van Dinter, Guoqing Chang, Yuki Nagai, Tadashi Machida, et al. Visualizing magnetic field-induced rotational electronic symmetry breaking in a spinel oxide superconductor. *arXiv preprint arXiv:2306.06711*, 2023.

[5] Rajesh V Chopdekar, Franklin J Wong, Yayoi Takamura, Elke Arenholz, and Yuri Suzuki. Growth and characterization of superconducting spinel oxide $LiTi_2O_4$ thin films. *Physica C: Superconductivity*, 469(21):1885–1891, 2009.

[6] S Mesoraca, JE Kleibeuker, B Prasad, JL MacManus-Driscoll, and MG Blamire. Lithium outdiffusion in liti2o4 thin films grown by pulsed laser deposition. *Journal of Crystal Growth*, 454:134–138, 2016.

[7] Akichika Kumatani, Takeo Ohsawa, Ryota Shimizu, Yoshitaka Takagi, Susumu Shiraki, and Taro Hitosugi. Growth processes of lithium titanate thin films deposited by using pulsed laser deposition. *Applied Physics Letters*, 101(12), 2012.

[8] Takayoshi Oshima, Kosuke Yokoyama, Mifuyu Niwa, and Akira Ohtomo. Pulsed-laser deposition of superconducting $LiTi_2O_4$ ultrathin films. *Journal of Crystal Growth*, 419:153–157, 2015.

[9] Richard E Honig. Vapor pressure data for the solid and liquid elements. *RCA review*, 30:285–305, 1969.

[10] Dongxue Du, Patrick J Strohbeen, Hanjong Paik, Chenyu Zhang, Konrad T Genser, Karin M Rabe, Paul M Voyles, Darrell G Schlom, and Jason K Kawasaki. Control of polymorphism during epitaxial growth of hyperferroelectric candidate LiZnSb on GaSb (111) b. *Journal of Vacuum Science & Technology B, Nanotechnology and Microelectronics: Materials, Processing, Measurement, and Phenomena*, 38(2):022208, 2020.

[11] Kui Jin, Ge He, Xiaohang Zhang, Shingo Maruyama, Shintaro Yasui, Richard Suchoski, Jongmoon Shin, Yeping Jiang, HS Yu, J Yuan, et al. Anomalous magnetoresistance in the spinel superconductor $LiTi_2O_4$. *Nature communications*, 6(1):7183, 2015.

[12] Mer Tinkham. Effect of fluxoid quantization on transitions of superconducting films. *Physical Review*, 129(6):2413, 1963.

[13] U Welp, WK Kwok, GW Crabtree, KG Vandervoort, and JZ Liu. Angular dependence of the upper critical field of $YBa_2Cu_3O_{7-\delta}$ single crystals. *Physical Review B*, 40(7):5263, 1989.

[14] Kazumi Maki and Toshihiko Tsuneto. Pauli paramagnetism and superconducting state. *Progress of Theoretical Physics*, 31(6):945–956, 1964.

[15] NR Werthamer, EF Helfand, and PC Hohenberg. Temperature and purity dependence of the superconducting critical field, H_{c2}. iii. electron spin and spin-orbit effects. *Physical Review*, 147(1):295, 1966.

[16] J.R. Kirtley, L. Paulius, A.J. Rosenberg, J.C. Palmstrom, C.M. Holland, E.M. Spanton, D. Schiessl, C.L. Jermain, J. Gibbons, Y.-K.-K. Fung, M.E. Huber, D.C. Ralph, M.B. Ketchen, G.W. Gibson, and K.A. Moler. Scanning squid susceptometers with sub-micron spatial resolution. *Rev Sci Instrum*, 87(9):093702, 2016.

[17] J.R. Kirtley, B. Kalisky, J.A. Bert, C. Bell, M. Kim, Y. Hikita, H.Y. Hwang, J.H. Nga, Y. Segal, F.J. Walker, C.H. Ahn, and K.A. Moler. Scanning squid susceptometry of a paramagnetic superconductor. *Physical Review B*, 85(22):224518, 2012.

[18] Mühlschlegel B. Die thermodynamischen funktionen des supraleiters. *Z. Physik*, 155:313–327, 1959.

[19] F Gross, BS Chandrasekhar, D Einzel, K Andres, PJ Hirschfeld, HR Ott, J Beuers, Z Fisk, and JL Smith. Anomalous temperature dependence of the magnetic field penetration depth in superconducting ube 13. *Zeitschrift für Physik B Condensed Matter*, 64:175–188, 1986.

[20] Yaoju Tarn, Mekhola Sinha, Christopher Pasco, Darrell G. Schlom, Tyrel M. McQueen, Kyle M. Shen, and Brendan D. Faeth. An algorithm for subtraction of doublet emission lines in angle-resolved photoemission spectroscopy. *Journal of Electron Spectroscopy and Related Phenomena*, 265:147323, 2023.

[21] Jialu Wang, Haiyang Yang, Linchao Ding, Wei You, Chuanying Xi, Jie Cheng, Zhixiang Shi, Chao Cao, Yongkang Luo, Zengwei Zhu, et al. Angle-dependent magnetoresistance and its implications for lifshitz transition in W_2As_3. *npj Quantum Materials*, 4(1):58, 2019.

[22] Carolina A. Marques, Philip A. E. Murgatroyd, Rosalba Fittipaldi, Weronika Osmolska, Brendan Edwards, Izidor Benedičič, Gesa-R. Siemann, Luke C. Rhodes, Sebastian Buchberger, Masahiro Naritsuka, Edgar Abarca-Morales, Daniel Halliday, Craig Polley, Mats Leandersson, Masafumi Horio, Johan Chang, Raja Arumugam, Mariateresa Lettieri, Veronica Granata, Antonio Vecchione, Phil D. C. King, and Peter Wahl. Spin-orbit coupling induced Van Hove singularity in proximity to a Lifshitz transition in $Sr_4Ru_3O_{10}$. *npj Quantum Materials*, 9(1):1–9, April 2024. Publisher: Nature Publishing Group.

[23] K. Jin, G. He, X. Zhang, S. Maruyama, S. Yasui, R. Suchoski, J. Shin, Y. Jiang, H. S. Yu, J. Yuan, L. Shan, F. V. Kusmartsev, R. L. Greene, and I. Takeuchi. Anomalous magnetoresistance in the spinel superconductor $LiTi_2O_4$. *Nature Communications*, 6(1):7183, May 2015. Publisher: Nature Publishing Group.

[24] Adam Kaminski and Helen M Fretwell. On the extraction of the self-energy from angle-resolved photoemission spectroscopy. *New Journal of Physics*, 7(1):98, apr 2005.

[25] Yuita Fujisawa, Anjana Krishnadas, Chia-Hsiu Hsu, Takahito Takeda, Sheng Liu, Markel Pardo-Almanza, Yukiko Obata, Dyon van Dinter, Kohei Yamagami, Guoqing Chang, et al. Imaging emergent exotic quasiparticle state in a frustrated transition metal oxide. *arXiv preprint arXiv:2306.06708*, 2023.

[26] G. Kresse and J. Hafner. Ab initio molecular dynamics for liquid metals. *Physical Review B*, 47:558–561, Jan 1993.

[27] G. Kresse and J. Furthmüller. Efficient iterative schemes for ab initio total-energy calculations using a plane-wave basis set. *Physical Review B*, 54:11169–11186, Oct 1996.

[28] G. Kresse and D. Joubert. From ultrasoft pseudopotentials to the projector augmented-wave method. *Physical Review B*, 59:1758–1775, Jan 1999.

[29] John P. Perdew, Kieron Burke, and Matthias Ernzerhof. Generalized gradient approximation made simple. *Phys. Rev. Lett.*, 77:3865–3868, Oct 1996.

[30] Paolo Giannozzi, Stefano Baroni, Nicola Bonini, Matteo Calandra, Roberto Car, Carlo Cavazzoni, Davide Ceresoli, Guido L Chiarotti, Matteo Cococcioni, Ismaila Dabo, Andrea Dal Corso, Stefano de Gironcoli, Stefano Fabris, Guido Fratesi, Ralph Gebauer, Uwe Gerstmann, Christos Gougoussis, Anton Kokalj, Michele Lazzeri, Layla Martin-Samos, Nicola Marzari, Francesco Mauri, Riccardo Mazzarello, Stefano Paolini, Alfredo Pasquarello, Lorenzo Paulatto, Carlo Sbraccia, Sandro Scandolo, Gabriele Sclauzero, Ari P Seitsonen, Alexander Smogunov, Paolo Umari, and Renata M Wentzcovitch. QUANTUM ESPRESSO: a modular and open-source software project for quantum simulations of materials. *Journal of Physics: Condensed Matter*, 21(39):395502, sep 2009.

[31] P Giannozzi, O Andreussi, T Brumme, O Bunau, M Buongiorno Nardelli, M Calandra, R Car, C Cavazzoni, D Ceresoli, M Cococcioni, N Colonna, I Carnimeo, A Dal Corso, S de Gironcoli, P Delugas, R A DiStasio, A Ferretti, A Floris, G Fratesi, G Fugallo, R Gebauer, U Gerstmann, F Giustino, T Gorni, J Jia, M Kawamura, H-Y Ko, A Kokalj, E Küçükbenli, M Lazzeri, M Marsili, N Marzari, F Mauri, N L Nguyen, H-V Nguyen, A Otero de-la Roza, L Paulatto, S Poncé, D Rocca, R Sabatini, B Santra, M Schlipf, A P Seitsonen, A Smogunov, I Timrov, T Thonhauser, P Umari, N Vast, X Wu, and S Baroni. Advanced capabilities for materials modelling with Quantum ESPRESSO. *Journal of Physics: Condensed Matter*, 29(46):465901, oct 2017.

[32] Arash A. Mostofi, Jonathan R. Yates, Giovanni Pizzi, Young-Su Lee, Ivo Souza, David Vanderbilt, and Nicola Marzari. An updated version of wannier90: A tool for obtaining maximally-localised Wannier functions. *Comput. Phys. Commun.*, 185(8):2309 – 2310, 2014.

[33] Stefano Baroni, Stefano de Gironcoli, Andrea Dal Corso, and Paolo Giannozzi. Phonons and related crystal properties from density-functional perturbation theory. *Rev. Mod. Phys.*, 73:515–562, Jul 2001.

[34] S. Poncé, E.R. Margine, C. Verdi, and F. Giustino. EPW: Electron–phonon coupling, transport and superconducting properties using maximally localized Wannier functions. *Computer Physics Communications*, 209:116 – 133, 2016.

[35] H. Lee, S. Poncé, K. Bushick, S. Hajinazar, J. Lafuente-Bartolome, J. Leveillee, C. Lian, J. Lihm, F. Macheda, H. Mori, H. Paudyal, W.H. Sio, S. Tiwari, M. Zacharias, X. Zhang, Nicola N. Bonini, E. Kioupakis, E.R. Margine, and F. Giustino. Electron–phonon physics from first principles using the EPW code. *npj Computational Materials*, 9:156, 2023.

[36] F. Giustino, M. L. Cohen, and S. G. Louie. Electron-phonon interaction using Wannier functions. *Phys. Rev. B*, 76:165108, 2007.

[37] L. J. P. Ament, M. Van Veenendaal, and J. Van Den Brink. Determining the electron-phonon coupling strength from Resonant Inelastic X-ray Scattering at transition metal L-edges. *EPL (Europhysics Letters)*, 95(2):27008, July 2011.

[38] S. Moser, S. Fatale, P. Krüger, H. Berger, P. Bugnon, A. Magrez, H. Niwa, J. Miyawaki, Y. Harada, and M. Grioni. Electron-phonon coupling in the bulk of anatase TiO_2 measured by resonant inelastic x-ray spectroscopy. *Physical Review Letters*, 115(9):096404, August 2015. Publisher: American Physical Society.

[39] JG Vale, CD Dashwood, E Paris, LSI Veiga, M Garcia-Fernandez, A Nag, A Walters, Ke-Jin Zhou, I-M Pietsch, Anton Jesche, et al. High-resolution resonant inelastic x-ray scattering study of the electron-phonon coupling in honeycomb α- Li_2IrO_3. *Physical Review B*, 100(22):224303, 2019.

[40] Y.L. Wang, G. Fabbris, M.P.M. Dean, and G. Kotliar. Edrixs: An open source toolkit for simulating spectra of resonant inelastic x-ray scattering. *Computer Physics Communications*, 243:151 – 165, 2019.

[41] Qizhi Li, Abhishek Nag, Xiquan Zheng, Fucong Chen, Jie Yuan, Kui Jin, Yi Lu, Ke-Jin Zhou, and Yingying Peng. Evolution of orbital excitations from insulating to superconducting $MgTi_2O_4$ films. *Physical Review B*, 107(12):L121108, March 2023.

[42] A. de la Torre, B. Zager, F. Bahrami, M. DiScala, J. R. Chamorro, M. H. Upton, G. Fabbris, D. Haskel, D. Casa, T. M. McQueen, F. Tafti, and K. W. Plumb. Enhanced hybridization in the electronic ground state of the intercalated honeycomb iridate $Ag_3LiIr_2O_6$. *Phys. Rev. B*, 104:L100416, Sep 2021.

[43] D. I. Khomskii, K. I. Kugel, A. O. Sboychakov, and S. V. Streltsov. Role of local geometry in the spin and orbital structure of transition metal compounds. *Journal of Experimental and Theoretical Physics*, 122(3):484–498, Mar 2016.

[44] Jun Sugiyama, Izumi Umegaki, Takeshi Uyama, Ryan ML McFadden, Susumu Shiraki, Taro Hitosugi, Zaher Salman, Hassan Saadaoui, Gerald D Morris, W Andrew MacFarlane, et al. Lithium diffusion in spinel $Li_4Ti_5O_12$ and $LiTi_2O_4$ films detected with Li 8 β-NMR. *Physical Review B*, 96(9):094402, 2017.

[45] Jun Sugiyama, Hiroshi Nozaki, Izumi Umegaki, Kazuhiko Mukai, Kazutoshi Miwa, Susumu Shiraki, Taro Hitosugi, Andreas Suter, Thomas Prokscha, Zaher Salman, et al. Li-ion diffusion in $Li_4Ti_5O_12$ and $LiTi_2O_4$ battery materials detected by muon spin spectroscopy. *Physical Review B*, 92(1):014417, 2015.

[46] Martin Månsson, Ola Kenji Forslund, Hiroshi Nozaki, Izumi Umegaki, Susumu Shiraki, Taro Hitosugi, Thomas Prokscha, Zaher Salman, Andreas Suter, Yasmine Sassa, et al. LE-SR study of superconductivity in the thin film battery material $LiTi_2O_4$. In *Proceedings of the 14th International Conference on Muon Spin Rotation, Relaxation and Resonance (μSR2017)*, page 011025, 2018.

[47] Jacob Madsen and Toma Susi. abTEM: Transmission electron microscopy from first principles. *Open Research Europe*, 1(24):13015, 2021.

[48] DC Johnston. Superconducting and normal state properties of $Li_{1+x}Ti_{2-x}O_4$ spinel compounds. i. preparation, crystallography, superconducting properties, electrical resistivity, dielectric behavior, and magnetic susceptibility. *Journal of Low Temperature Physics*, 25:145–175, 1976.

[49] C Chen, M Spears, F Wondre, and J Ryan. Crystal growth and superconductivity of $LiTi_2O_4$ and $Li_{1+1/3}Ti_{2-1/3}O_4$. *Journal of Crystal Growth*, 250(1-2):139–145, 2003.

[50] D. Chen, Y.-L. Jia, T.-T. Zhang, Z. Fang, K. Jin, P. Richard, and H. Ding. Raman study of electron-phonon coupling in thin films of the spinel oxide superconductor $LiTi_2O_4$. *Physical Review B*, 96(9):094501, September 2017. Publisher: American Physical Society.

[51] Yanwei Cao, Xiaoran Liu, M Kareev, D Choudhury, S Middey, D Meyers, J-W Kim, PJ Ryan, JW Freeland, and J Chakhalian. Engineered mott ground state in a $LaTiO_{3+\delta}/LaNiO_3$ heterostructure. *Nature Communications*, 7(1):10418, 2016.

[52] Wonkyung Ra, Masanobu Nakayama, Yoshiharu Uchimoto, and Masataka Wakihara. Experimental and computational study of the electronic structural changes in $LiTi_2O_4$ spinel compounds upon electrochemical Li insertion reactions. *The Journal of Physical Chemistry B*, 109(3):1130–1134, 2005.

[53] Fongchi Xu, YC Liao, MJ Wang, CT Wu, KF Chiu, and MK Wu. The preparation effect of $Li_{1+x}Ti_2O_4$ and its aging effect. *Journal of low temperature physics*, 131(3):569–574, 2003.

[54] Takashi Inukai, Toshiaki Murakami, and Takahiro Inamura. Aging effects of Li-Ti-O superconducting compounds. *Japanese Journal of Applied Physics*, 20(9):L681, 1981.